Mathematics

AIMS Mathematics, 11(6): 15765–15796.
DOI: 10.3934/math.2026649
Received: 08 March 2026
Revised: 04 April 2026
Accepted: 23 April 2026
Published: 04 June 2026

https://www.aimspress.com/journal/Math

Research article

Constrained flows of fluids with chemically reacting pollutants through porous media with linear and quadratic drag

Rogério P. S. Gama[1], Douglas M. Andrade[1], Rogério M. Saldanha da Gama[1,*], Felipe B. de Freitas Rachid[2], Heraldo S. da Costa Mattos[2] and Maria L. Martins-Costa[2]

[1] Mechanical Engineering Graduate Program (FEN), Universidade do Estado do Rio de Janeiro, 524 Rua São Francisco Xavier, Rio de Janeiro, RJ 20550-013, Brazil
[2] Laboratory of Theoretical and Applied Mechanics (LMTA) Mechanical Engineering Graduate Program (TEM-PGMEC), Universidade Federal Fluminense, 156 Rua Passo da Pátria, Niterói, RJ 24210-240, Brazil

* **Correspondence:** Email: rsggama@gmail.com.

Abstract: Constrained Newtonian fluids containing reacting pollutants flowing through porous media were modeled using a continuum theory of mixtures approach, accounting for viscous linear and quadratic drag terms. The work considered very low pollutant concentrations and similar mass densities for the fluid and all the pollutant constituents. These constituents may undergo chemical reactions among themselves, but they do not react with the fluid constituent. In this case, equal velocities for the pollutant constituents and the fluid constituent may be assumed. A solid constituent (the porous matrix, rigid and at rest), an inert gas (to account for the mixture's compressibility), an incompressible fluid (the fluid constituent), and N pollutant constituents compose the mixture. The model encompasses the mass equations for the fluid constituent and the N-pollutant constituents, as well as the fluid constituent's momentum balance. The Glimm scheme, associated with an operator-splitting technique, was used to advance in time. The complete solution to the associated Riemann problem was presented. The numerical results show the evolution of the fluid constituent's velocity and saturation, and the pollutant constituents' concentrations in the mixture for selected initial data, accounting for Darcy and Forchheimer drag terms, and chemical reactions among the pollutants. The novelty lies in the combination of linear and quadratic drag terms with simple chemical reactions among the pollutants, the use of a new constitutive relation for pressure (accounting for kinematic constraints), and a new protocol for the Glimm scheme.

Keywords: constrained flows through porous media; chemical reactions; Glimm's scheme; operator-splitting; mixture theory
Mathematics Subject Classification: 35L65, 76S99

1. Introduction

Flows through porous media are relevant to engineering applications and are adequately described by a mixture theory viewpoint (see [1] and the references therein).

There is a wide variety of transport phenomena in porous media applications that are environmentally relevant, many of them involving chemical reactions [2,3], such as capturing and storing atmospheric carbon dioxide, or the penetration of chemicals into the soil. There may be contaminants present in groundwater flows migrating through the aquifers [4,5]. Regarding oil and gas applications, transport in porous media is relevant for simulating oil reservoir flow, natural gas production, or enhanced oil recovery [4,6]. Further applications include drying, filtration, agricultural land drainage, mass transfer through membranes, geothermal energy harvesting and management, and even fuel cells, in which electricity and heat are generated by electrochemical reactions originating from hydrocarbon fuels and oxidants flowing through porous media [7,8].

Aiming to represent polluted fluid flows through porous media, a subject of broad engineering applications, this work studies the unsaturated flow of an incompressible Newtonian fluid containing suspended pollutants (which react chemically with one another). The mixture consists of a fluid constituent and N-pollutant constituents embedded in an almost rigid porous matrix, represented by the solid constituent. The unsaturated porous matrix is subject to a unilateral constraint that allows ultra-small, controlled supersaturation of the matrix.

The continuum theory of mixtures departs from the concept of superposed continuous constituents of a given mixture (so that each spatial point of the mixture is occupied, simultaneously, by all the constituents of the mixture) under a macroscopic description, being endowed with apparent thermomechanical independence, thus requiring additional terms, internal source terms, absent in a classical continuum mechanical description, to account for the interaction among the constituents [9–11]. This approach requires that the conservation equations be satisfied by all constituents of the mixture and by the mixture as a whole [9,12,13]. The mechanical model is built by combining conservation equations with systematically proposed constitutive hypotheses [14–16].

Flows through porous media have presented many important developments in recent years. Examples are magnetohydrodynamic flows, considered by Abdelsalam et al. [17] and Bhatti et al. [18]. The former solved the complex partial differential equations that model fluid flow and heat transfer, including similarity transformations and the homotopy perturbation method, while the latter used Lie symmetry and Chebyshev spectral techniques to solve the resulting problem. The magnetized nanofluid flow saturated in a non-Darcian medium was considered by Bhatti et al. [19], using Buongiorno and Arrhenius models, and employing Von Karman's methodology and a generalized differential quadrature technique in the solution.

A mixture of N+3 constituents is considered: a porous medium at rest (the solid constituent), an inert gas with very low density (included to allow the compressibility of the mixture), a Newtonian fluid (from now on called the fluid constituent) flowing through the porous medium, and N pollutants suspended in the mixture. The pollutants react among themselves but not with the fluid and have mass

densities of the same order of magnitude as the fluid's. Assuming small concentrations for the pollutant constituents leads to the assumption that their velocities are approximately equal to the main liquid's velocity (the fluid constituent), which, in turn, is approximately equal to the velocity of the mixture. So, the balance equations to be satisfied are the mass balances for the N pollutant constituents and for the fluid constituent. In contrast, the fluid constituent must satisfy the momentum equation. (Note that the solid constituent is assumed to be almost rigid and at rest, and the gas constituent has negligible density.)

This work could be regarded as a sequence of da Gama et al. [20] and Martins-Costa et al. [21]. The former reviews constrained hyperbolic flows through porous media, employing a constitutive equation for the pressure, a non-negative function of saturation with a continuous, increasing first derivative. The problem remains hyperbolic even at very small supersaturation, resulting in only a tiny deformation of the porous matrix. The nonlinear hyperbolic problem is simulated by Glimm's method, and the complete (exact) solution of the associated Riemann problem (employed to build the Glimm scheme) is presented. In [21], the mechanical model yields a non-linear, non-homogeneous hyperbolic problem that is simulated by combining the Glimm scheme with an operator-splitting technique, separating the time-evolving part from the purely hyperbolic one. It is important to note that these works considered a mixture of three constituents, and the non-homogeneous terms in [21] account for linear and quadratic drag terms.

In the present work, there are N+3 continuous constituents because N pollutant constituents are reacting among themselves, and the numerical model for the resulting N+2 equations also combines Glimm's scheme with operator-splitting to deal with linear and quadratic drag terms and the pollutants' mass variation resulting from the chemical reactions. This work's originality lies in applying operator-splitting to handle the mass-variation terms arising from chemical reactions among the pollutants, as well as in a variant of the Glimm scheme that involves several random choices at each time step.

2. Mechanical model

The mechanical model for isothermal unsaturated flow of a pseudo-mixture (composed of an incompressible Newtonian fluid and N pollutants) through a porous matrix within a mixture theory approach considers N+3 continuous constituents. The almost rigid porous matrix, represented by the solid constituent (at rest) and the negligible mass density gas constituent (included to consider the mixture's compressibility), do not need to satisfy mass and momentum balance equations. The pseudo-mixture must satisfy them exclusively, representing the so-called fluid constituents and the pollutant constituents. Also, since the concentration of all the N pollutants suspended in the pseudo mixture is small and their mass density is of the same order of magnitude as the main liquid, the mass balance must be satisfied by N pollutant constituents (that react among themselves, but not with the fluid constituent) and by the fluid constituent. In contrast, the momentum balance must be satisfied by the fluid constituent only. It should be noted that the N pollutant constituents' velocities are approximately equal to the fluid constituent velocity. For convenience, first, the pollutant concentration in the mixture ω_i is defined, considering the main fluid density for an incompressible continuum medium ρ_F, the i-th pollutant density in the mixture ρ_i, and the porosity ε, which we define as

$$\omega_i = \frac{\rho_i}{\varepsilon \rho_F}. \tag{2.1}$$

In this case, the balance equations–fluid constituent mass and momentum balances and the N pollutant constituents mass balances [9,11,12] are given by

$$\begin{cases} \dfrac{\partial \rho_f}{\partial t} + \operatorname{div}\left(\rho_f \mathbf{v}_f\right) = 0, \\ \rho_f \left[\dfrac{\partial \mathbf{v}_f}{\partial t} + \left(\operatorname{grad} \mathbf{v}_f\right)\mathbf{v}_f\right] = \operatorname{div} \mathbf{T}_f + \mathbf{m}_f + \rho_f \mathbf{g}, \\ \dfrac{\partial \omega_i}{\partial t} + \operatorname{div}\left(\omega_i \mathbf{v}_f\right) = r_i, \qquad i = 1, N, \end{cases} \tag{2.2}$$

where r_i represents the mass generation rate of the i-th pollutant constituent. The gravitational effects will be neglected in this work.

Note that the saturation ψ, given by the ratio between the fluid fraction ϕ and the porous matrix porosity ε (measured under a continuum mechanics viewpoint) cannot surpass unity, but a tiny supersaturation is allowed in this work, provoking a tiny porous matrix deformation. We propose an "enlarged" saturation, φ, given by

$$\varphi = \frac{\phi}{\varepsilon + \delta} \quad \text{satisfying } \psi = \frac{\phi}{\varepsilon} = \frac{\rho_f}{\varepsilon \rho_F} < 1 + \frac{\delta}{\varepsilon}, \quad \delta << \varepsilon, \tag{2.3}$$

where δ is a very small positive constant.

The partial stress tensor acting on the fluid constituent $\mathbf{T}_f$ is assumed to be proportional to the pressure and to the strain rate tensor acting on the fluid constituent [22], but Allen [23] stated that the normal stresses were dominant, leading to a constitutive assumption of $\mathbf{T}_f$ being proportional to the pressure acting on the fluid constituent $\bar{p}$:

$$\mathbf{T}_f = -\bar{p}\,\mathbf{1}, \quad \bar{p} = \hat{f}(\varphi). \tag{2.4}$$

The force $\mathbf{m}_f$ represents a momentum source acting on the fluid constituent due to its interaction with the remaining constituents of the mixture. It represents the drag force, given by a linear term depending on the fluid constituent velocity, usually known as the Darcy term, a quadratic term also depending on the square of the fluid constituent velocity, known as the Forchheimer term [21,24,25], and a term attempting to model the capillary forces effect under a mixture theory viewpoint, accounting for the strong dependency of unsaturated flows on saturation and the saturation gradient [22,26,27]. Note that the solid constituent is at rest, the gas constituent has negligible mass, and the pollutant constituents' velocity is assumed to be equal to the fluid constituent velocity $\mathbf{v}_f$, so the dependency is on the velocity $\mathbf{v}_f$ and not on the relative velocity. The source $\mathbf{m}_f$ is

$$\mathbf{m}_f = -\gamma_1 \varphi^2 \mathbf{v}_f - \gamma_2 \varphi^2 \left|\mathbf{v}_f\right| \mathbf{v}_f - \frac{\mu_f \varepsilon^2 D}{K} \nabla \varphi, \text{ with } \gamma_1 = \frac{\mu_f \varepsilon^2}{\rho_f K} \text{ and } \gamma_2 = \frac{\varepsilon^2 \bar{F}}{K^{1/2}}, \tag{2.5}$$

where μ_f represents the fluid viscosity, $\bar{F}$ is the Forchheimer number, K is the porous matrix specific permeability, and the variable D is a diffusion coefficient. All variables are measured under a continuum mechanics approach.

In Eq (2.5), the first two terms represent the drag force. The former is usually known as the Darcy term (exhibiting a linear dependency on the fluid constituent velocity) and the latter as the Forchheimer term (exhibiting a quadratic dependency on the fluid constituent velocity). Their influence on the flow will be considered by varying their coefficients γ_1 and γ_2, respectively. The last term aims to represent the effect of capillary forces and is absent in saturated flow.

We suppose that all variables depend solely on the time t and on the coordinate of the flow direction x, and make the velocity in the flow direction $\mathbf{v}_f \equiv u$. Also, we assume the absence of body force terms in the flow direction and a convenient relation for the pressure, which is

$$\frac{\partial \overline{p}}{\partial x} + \frac{\mu_f \varepsilon D \rho_f}{K} \frac{\partial \varphi}{\partial x} = \frac{\partial p}{\partial x}. \tag{2.6}$$

The system may be written as

$$\begin{cases} \dfrac{\partial \varphi}{\partial t} + \dfrac{\partial}{\partial x}(\varphi u) = 0, \\ \dfrac{\partial}{\partial t}(\varphi u) + \dfrac{\partial}{\partial x}\left(\varphi u^2 + p\right) = -\gamma_1 \varphi^2 u - \gamma_2 \varphi^2 |u| u, \quad \text{with} \quad p = \hat{p}(\varphi), \\ \dfrac{\partial \omega_i}{\partial t} + \dfrac{\partial}{\partial x}(\omega_i u) = r_i, \quad i = 1, N. \end{cases} \tag{2.7}$$

Note that the saturation φ and pollutant concentrations ω_i are always positive variables. Without loss of generality, from Eq (2.6) on, we consider t a dimensionless time (the original time divided by one second) and x a dimensionless position (the original position divided by one meter).

It should be noted that combining very low concentrations of pollutant constituents with densities of the same order as the fluid constituent (forming the pseudo-mixture) is a simplifying assumption, with some limitations. However, to the best of our knowledge, a problem combining Darcy-Forchheimer drag terms with pollutant generation in a mixture theory context has not been previously addressed. Besides, a constrained functional relationship between pressure and saturation ensures that the problem always remains hyperbolic and preserves its physical meaning.

This work considers numerical simulations with three pollutant constituents. If the rate of a pollutant constituents' mass generation depends linearly on the pollutant concentrations, $r_i = \hat{r}_i(\omega_j)$, the last equation in Eq (2.7), representing the pollutant constituents' mass conservation, would give rise to the following system (with the simple linear pollutant constituents' mass generation rate proposed in this work):

$$\begin{cases} \dfrac{\partial \omega_1}{\partial t} + \dfrac{\partial}{\partial x}(\omega_1 u) = \dfrac{r_1}{\varepsilon \rho_F}, \\ \dfrac{\partial \omega_2}{\partial t} + \dfrac{\partial}{\partial x}(\omega_2 u) = \dfrac{r_2}{\varepsilon \rho_F}, \\ \dfrac{\partial \omega_3}{\partial t} + \dfrac{\partial}{\partial x}(\omega_3 u) = -\dfrac{(r_1 + r_2)}{\varepsilon \rho_F}, \end{cases} \quad \text{or} \quad \begin{cases} \dfrac{\partial \omega_1}{\partial t} + \dfrac{\partial}{\partial x}(\omega_1 u) = -\alpha \omega_1, \\ \dfrac{\partial \omega_2}{\partial t} + \dfrac{\partial}{\partial x}(\omega_2 u) = -\beta \omega_2, \\ \dfrac{\partial \omega_3}{\partial t} + \dfrac{\partial}{\partial x}(\omega_3 u) = \alpha \omega_1 + \beta \omega_2. \end{cases} \tag{2.8}$$

Note that although only three pollutants are considered in the simulations of this work, the complete exact solution of the associated Riemann problem (presented in the Appendix) is valid for any number of pollutants *N*. Also, the pollutants react among themselves but do not react with the fluid constituent or with the solid constituent that represents the porous matrix.

At this point, the kinematic constraint should be addressed. Physically, the quantity of incompressible fluid contained in a pore cannot have a volume larger than the pore's volume. To ensure that, the pressure p and the "enlarged" saturation φ defined by Eq (2.3) should satisfy the following limits:

$$\lim_{\varphi \to 1} p = +\infty \qquad \text{and} \qquad \lim_{p \to +\infty} \varphi = 1. \tag{2.9}$$

Taking (2.3) and (2.9) into account, the following constitutive relation for the pressure is considered:

$$p = \hat{p}(\varphi) = \frac{\varphi^3}{3(1-\varphi)^3}. \tag{2.10}$$

Note that Eq (2.10) satisfies the conditions imposed by Eq (2.9), as well as the kinematic constraints. So, this proposed relation accounts for the kinematic constraint.

3. Numerical methodology

Equation (2.7) represents a nonlinear, non-homogeneous hyperbolic system. The numerical simulation combines Glimm's scheme to simulate the homogeneous portion of the hyperbolic operator with an operator-splitting procedure to deal with the non-homogeneous portion present in the last three equations of Eq (2.7), explicitly presented in Eq (2.8), as well as the Darcy and Forchheimer terms shown in the constitutive relation for the momentum source $\mathbf{m}_f$ presented in Eq (2.5).

Glimm's system marches on time, employing the solution to a certain number of Riemann problems (which can be chosen in advance). The complete (closed) solution for the associated Riemann problem is presented in the Appendix.

3.1. The implementation of the Glimm method

The semi-analytical Glimm method [28,29] approximates initial value problems by advancing from a given time instant t_n to the subsequent one t_{n+1}, employing a chosen number of associated Riemann problems. First, the arbitrary initial condition (a function of the position) is approximated by piecewise constant functions, selected using a randomly chosen number θ, such that

$$\begin{aligned} &f(x) \approx f(x_j + \theta \Delta x) = \text{constant}, \\ &\text{for } x_j < x < x_j + \Delta x = x_{j+1}, \qquad \Delta x = x_{j+1} - x_j, \end{aligned} \tag{3.1}$$

with θ being a random number in the interval $(-1/2,\ +1/2)$. From this random selection, a step function is constructed, which allows the use of the exact solution of the associated Riemann problem (see the Appendix).

In the sequence, the associated Riemann problem with a step function as the initial condition is solved for each two consecutive intervals. Note that when the approximation at the time t_{n+1} is obtained, a new random choice must be made. To guarantee the absence of interaction between adjacent Riemann problems, ensuring uniqueness, the Courant-Friedrichs-Lewy (CFL) [30] condition must be satisfied. In other words:

$$t_{n+1} < \frac{\Delta x}{2|\lambda|_{MAX}} + t_n, \tag{3.2}$$

in which $|\lambda|_{MAX}$ represents the maximum propagation speed, considering all the associated Riemann problems.

For every two consecutive intervals, a Riemann problem can be constructed, whose solution is previously known, centered on each of the x_j's. Considering same-width steps, the j-th Riemann problem, which will provide the approximation for the instant t_n, is given by the combination of the homogeneous associated part of Eq (2.7) with the initial conditions, namely:

$$\begin{aligned}
&\frac{\partial \varphi}{\partial t} + \frac{\partial}{\partial x}(\varphi u) = 0, \\
&\frac{\partial}{\partial t}(\varphi u) + \frac{\partial}{\partial x}(\varphi u^2 + p) = 0, \quad p = \hat{p}(\varphi) = \frac{\varphi^3}{3(1-\varphi)^3}, \\
&\frac{\partial \omega_i}{\partial t} + \frac{\partial}{\partial x}(\omega_i u) = 0, \quad i = 1,3, \\
&(\varphi, u, \omega_i) = \begin{cases} (\varphi, u, \omega_i)\big|_{j-1}, & -\infty < x - x_j < 0, \quad t - t_n = 0, \\ (\varphi, u, \omega_i)\big|_{j}, & 0 < x - x_j < \infty, \quad t - t_n = 0, \end{cases} \qquad i = 1,3.
\end{aligned} \tag{3.3}$$

The initial conditions stated in the last equations of Eq (3.3) could be conveniently expressed as

$$\begin{aligned}
&\mathbf{v}(x,0) = \mathbf{v}^0(x) \text{ with } \mathbf{v} = [\varphi, u, \omega_i]^T, \quad i = 1,3, \\
&\Rightarrow \mathbf{v}^0(x) = (\varphi, u, \omega_i) = \begin{cases} (\varphi_L, u_L, \omega_{i_L}), & -\infty < x < 0, \quad t = 0, \\ (\varphi_R, u_R, \omega_{i_R}), & 0 < x < \infty, \quad t = 0. \end{cases}
\end{aligned} \tag{3.4}$$

The spatial domain is discretized into computational cells defined by real intervals of equal width Δx, centered at x_j. For each spatial interval, the left and right extremes are given, respectively, by

$$x_{j-1/2} = x_j - \frac{\Delta x}{2}, \qquad x_{j+1/2} = x_j + \frac{\Delta x}{2}; \qquad j = 1, 2M - 1. \tag{3.5}$$

The initial condition is replaced by a piecewise-constant function constructed via a random-choice procedure. In other words, the initial condition is approximated by a function consisting of $2M$ constant parts with equal width. This procedure gives rise to $2M - 1$ Riemann problems, each one centered at a point x_j, with the left state given by $\mathbf{v}_j^n$ and the right state given by $\mathbf{v}_{j+1}^n$. The number

M is chosen in such a way that, at the extremes of the whole interval, $\mathbf{v}(x,0) = \mathbf{v}(x,t)$.

The solution evolves from the information at the time t_n to a subsequent time instant given by $t_{n+1} = t_n + \Delta t$, with $\Delta t > 0$.

The pairs $\mathbf{v}_j^n$ and $\mathbf{v}_{j+1}^n$ define the states on the left and on the right for the local Riemann problem centered in x_j (with an available exact solution).

The solution advances from time t_n to time $t_{n+1} = t_n + \Delta t$ satisfying the CFL condition.

In the sequence, using a random number θ within the interval $(-1/2,1/2)$, the solution of the Riemann problem j gives rise to a new step function as follows:

$$\mathbf{v}^{n+1} = \begin{cases} \mathbf{v}^{n+1}\left(\theta\Delta x + x_j\right) = \mathbf{v}_{j+1}^{n+1} = constant, \quad for\ x \in \left(x_j, x_{j+1}\right)\ if\ \ 0 \le \theta < \dfrac{1}{2}, \\ \mathbf{v}^{n+1}\left(\theta\Delta x + x_j\right) = \mathbf{v}_{j}^{n+1} = constant, \quad for\ x \in \left(x_{j-1}, x_j\right)\ if\ \ -\dfrac{1}{2} \le \theta < 0, \end{cases} \tag{3.6}$$

at the time t^{n+1}.

Olivier and Grönig [31] stated that the momentary repetition of the signal of the random number θ might provoke errors in the positions of shock or rarefaction waves. For instance, this could be observed in the case of an always positive or a consistently negative number θ. To avoid this problem, four distinct sequences are considered in this work when implementing the Glimm scheme, aiming at minimizing any error in the positions of shocks or rarefaction waves. In each time step from t_n to t_{n+1}, four different solutions are obtained from Glimm's method, all of which are considered in the same spatial interval. The first one originates from the sequence, which is called $\{+\theta_n\}$. It is denoted by $\left(\mathbf{v}_j^{n+1}\right)_+^1$ and given by

$$\begin{aligned} \left(\mathbf{v}_{j+1}^{n+1}\right)_+^1 &= \mathbf{v}^{n+1}\left(\theta_n\Delta x + x_j\right) = constant, \quad for\ x \in \left(x_j, x_{j+1}\right)\ if\ \ 0 \le \theta_n < \frac{1}{2}, \\ \left(\mathbf{v}_{j}^{n+1}\right)_+^1 &= \mathbf{v}^{n+1}\left(\theta_n\Delta x + x_j\right) = constant, \quad for\ x \in \left(x_{j-1}, x_j\right)\ if\ \ -\frac{1}{2} \le \theta_n < 0. \end{aligned} \tag{3.7}$$

The second solution uses the sequence called $\{-\theta_n\}$, the mirrored image of the sequence $\{+\theta_n\}$. It is expressed by $\left(\mathbf{v}_j^{n+1}\right)_-^1$ and given by

$$\begin{aligned} \left(\mathbf{v}_{j}^{n+1}\right)_-^1 &= \mathbf{v}^{n+1}\left(\theta_n\Delta x + x_j\right) = constant, \quad for\ x \in \left(x_{j-1}, x_j\right)\ if\ \ 0 \le -\theta_n < \frac{1}{2}, \\ \left(\mathbf{v}_{j+1}^{n+1}\right)_-^1 &= \mathbf{v}^{n+1}\left(\theta_n\Delta x + x_j\right) = constant, \quad for\ x \in \left(x_{j}, x_{j+1}\right)\ if\ \ -\frac{1}{2} \le -\theta_n < 0. \end{aligned} \tag{3.8}$$

The third and fourth solutions are obtained analogously from the sequences labeled $\{+\theta_n\}$ and their symmetric sequence labeled $\{-\theta_n\}$. They are expressed respectively by

$$\begin{aligned}
&\left(\mathbf{v}_{j+1}^{n+1}\right)_{+}^{2}=\mathbf{v}^{n+1}\left(\theta_n\Delta x+x_j\right)=constant, \qquad for\ x\in\left(x_j,x_{j+1}\right)\ if\ 0\le\theta_n<\frac{1}{2},\\
&\left(\mathbf{v}_{j}^{n+1}\right)_{+}^{2}=\mathbf{v}^{n+1}\left(\theta_n\Delta x+x_j\right)=constant, \qquad for\ x\in\left(x_{j-1},x_j\right)\ if\ -\frac{1}{2}\le\theta_n<0,
\end{aligned} \tag{3.9}$$

$$\begin{aligned}
&\left(\mathbf{v}_{j}^{n+1}\right)_{-}^{2}=\mathbf{v}^{n+1}\left(\theta_n\Delta x+x_j\right)=constant, \qquad for\ x\in\left(x_{j-1},x_j\right)\ if\ 0\le-\theta_n<\frac{1}{2},\\
&\left(\mathbf{v}_{j+1}^{n+1}\right)_{-}^{2}=\mathbf{v}^{n+1}\left(\theta_n\Delta x+x_j\right)=constant, \qquad for\ x\in\left(x_j,x_{j+1}\right)\ if\ -\frac{1}{2}\le-\theta_n<0.
\end{aligned} \tag{3.10}$$

Finally, a solution independent of the θ_n sign is obtained from the average (arithmetic mean), considering the four previously obtained solutions:

$$\overline{\mathbf{v}}_j^{n+1}=\frac{\left(\mathbf{v}_j^{n+1}\right)_{+}^{1}+\left(\mathbf{v}_j^{n+1}\right)_{-}^{1}+\left(\mathbf{v}_j^{n+1}\right)_{+}^{2}+\left(\mathbf{v}_j^{n+1}\right)_{-}^{2}}{4}. \tag{3.11}$$

It should be noted that the Glimm method [28, 29] preserves the magnitude and the position of the shocks. The solution, considering four concomitant random choices at each time advance, presented in Eq (3.11), avoids possible errors in the positions of shock or rarefaction waves [31], thus enhancing the precision already ensured by the Glimm scheme.

3.2. The operator splitting-scheme

The operator-splitting procedure is required to deal with the nonlinear non-homogeneous system associated with Eq (2.7). First, departing from the time instant t_n, a time advance is made using the Glimm method previously described, considering the homogeneous associated system given by Eq (3.13) until the time instant t_{n+1} is reached and the solution independent of the θ_n sign is given by Eq (3.11). This could be associated with a "prediction" step. In the sequence, the approximation for the functions φ, u, and ω_i at the time instant t_{n+1} is considered as an initial condition and a new time advance from t_n until t_{n+1}, using the same time interval $\Delta t=t_{n+1}-t_n$ used for approximating the system by the Glimm method. This "correction" step would be performed with the following system:

$$\begin{aligned}
&\frac{\partial\varphi}{\partial t}=0,\quad \frac{\partial}{\partial t}\left(\varphi u\right)=m\,,\quad m=-\gamma_1\varphi^2u-\gamma_2\varphi^2\left|u\right|u,\\
&\frac{\partial\omega_i}{\partial t}=r_i,\quad i=1,3,\\
&\begin{cases}
\dfrac{\partial\omega_1}{\partial t}=-\alpha\omega_1,\\
\dfrac{\partial\omega_2}{\partial t}=-\beta\omega_2,\\
\dfrac{\partial\omega_3}{\partial t}=\alpha\omega_1+\beta\omega_2.
\end{cases}
\end{aligned} \tag{3.12}$$

The result obtained from Eq (3.12) is an approximation at the time instant t_{n+1}. In the sequence, a new random choice is required.

The protocol described requires that the time interval $t_{n+1} - t_n$ be sufficiently small to allow the simultaneous effects to be treated as sequential ones. In these cases, the product $(t_{n+1} - t_n)r_i$ must be sufficiently small to allow the operator-splitting procedure.

The system described in Eq (3.12) is approximated by a Euler scheme for time advancement. Since the function φ is time-independent, the approximation is given by

$$\begin{aligned} &\varphi\big|_{t_{n+1}} = \varphi\big|_{t_n}, \\ &\left(\varphi\big|_{t_n}\right)u\Big|_{t_{n+1}} = \left(\varphi\big|_{t_n}\right)u\big|_{t_n} + \left(m\big|_{t_n}\right)\left(t_{n+1} - t_n\right), \\ &\omega_i\big|_{t_{n+1}} = \omega_i\big|_{t_n} + \left(r_i\big|_{t_n}\right)\left(t_{n+1} - t_n\right), \quad i = 1,3. \end{aligned} \tag{3.13}$$

The results obtained from Eq (3.13) are the numerical approximations of the results for the variables (φ, u, ω_i) at the time instant t_{n+1}.

Note that a global validation of the previously described methodology was performed with the mass conservation equations: First, the mass of the fluid constituent is conserved at every time instant (with an uncertainty of less than 1%). The simple model adopted for the pollutant constituents allows that a reaction between two constituents, given their concentrations ω_1 and ω_2 at the initial instant, gives rise to a certain amount of a third constituent ω_3 (with zero concentration at the initial instant) at subsequent time instants. So, this also allows verification of the mass conservation equations for all three pollutant constituents (with an uncertainty of less than 1%) at every time instant.

In addition, the cases presented in Figures 1–5, considering $\alpha = \beta = \gamma_1 = \gamma_2 = 0.0$, were simulated. These results were compared to the exact solution provided in the Appendix, lending strong support for validating the numerical results.

4. Numerical results

Figures 1–4 present some results, illustrating a direct comparison between the initial condition and the concentration of the suspended constituents at each instant of time, taking into account the effects of the Darcy (proportional to the γ_1 coefficient) and Forchheimer (proportional to the γ_2 coefficient) drag terms, presented in Eq (3.12), for selected instants of time, on saturation, velocity, and concentrations ω_1, ω_2, and ω_3. The dotted lines (associated with the variables ω_1, ω_2, and ω_3), whenever present, indicate the initial condition, for comparison purposes, at each instant of time.

Figure 1 considers a constant value for the saturation ($\varphi = 0.6$), a step function for the fluid constituent velocity ($u = +1$ for $x < 0$ and $u = -1$ for $x > 0$), and distinct constant values for the pollutants' concentration ($\omega_1 = 0.3$, $\omega_2 = 0.2$, and $\omega_3 = 0$), as well as a zero-friction factor ($\gamma_1 = \gamma_2 = 0.0$), so that the behavior is only affected by the high reaction rate among the pollutants with $\alpha = \beta = 0.05$.

Figure 2 considers the same initial conditions employed in Figure 1, but now the friction is accounted for, with $\gamma_1 = \gamma_2 = 0.5$. The same high reaction rate among the pollutants ($\alpha = \beta = 0.05$) used in Figure 1 was used, allowing us to verify the very strong effect of the Darcy and the Forchheimer terms, the friction terms, in all considered parameters. This influence is even more pronounced in pollutant concentrations.

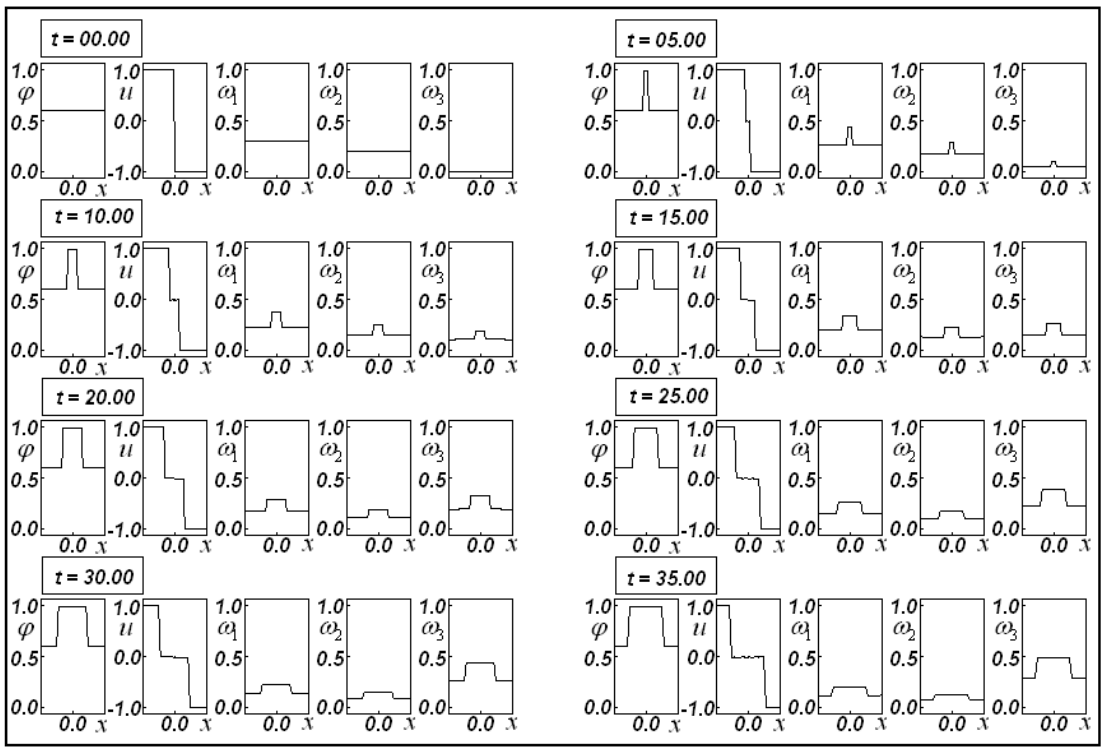

Figure 1. Evolution of saturation φ, velocity u, and the pollutants' concentrations $(\omega_1, \omega_2, \omega_3)$ for $\alpha = \beta = 0.05$ and $\gamma_1 = \gamma_2 = 0.0$.

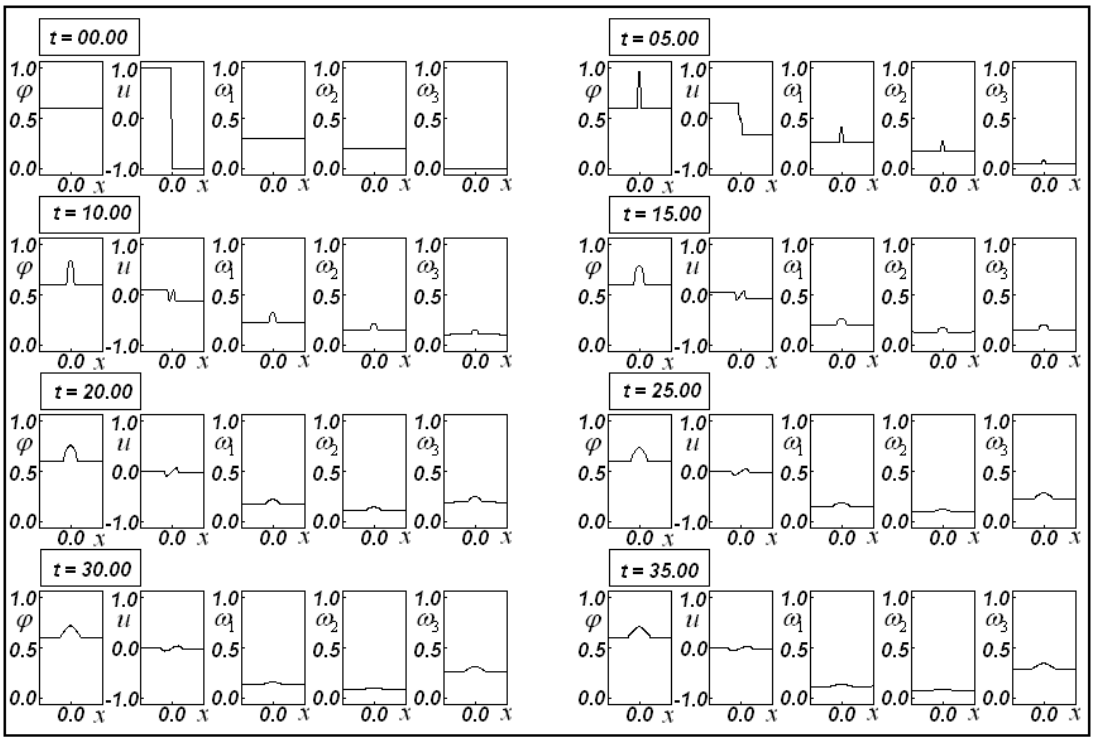

Figure 2. Evolution of saturation φ, velocity u, and the pollutants' concentrations $(\omega_1, \omega_2, \omega_3)$ for $\alpha = \beta = 0.05$ and $\gamma_1 = \gamma_2 = 0.5$.

In Figure 3, the initial data consists of a step function for the saturation (with $\varphi = 0.5$ for $x < 0$ and $\varphi = 0.2$ for $x > 0$), zero velocity for the fluid constituent, and the same pollutants' concentration used to sketch Figures 1 and 2 ($\alpha = \beta = 0.05$). Like in Figure 1, the friction is neglected ($\gamma_1 = \gamma_2 = 0.0$) and the dotted lines (associated with the variables ω_1, ω_2, and ω_3) indicate the initial condition, for comparison purposes, at each instant of time. This interesting feature allows the qualitative evaluation of mass conservation.

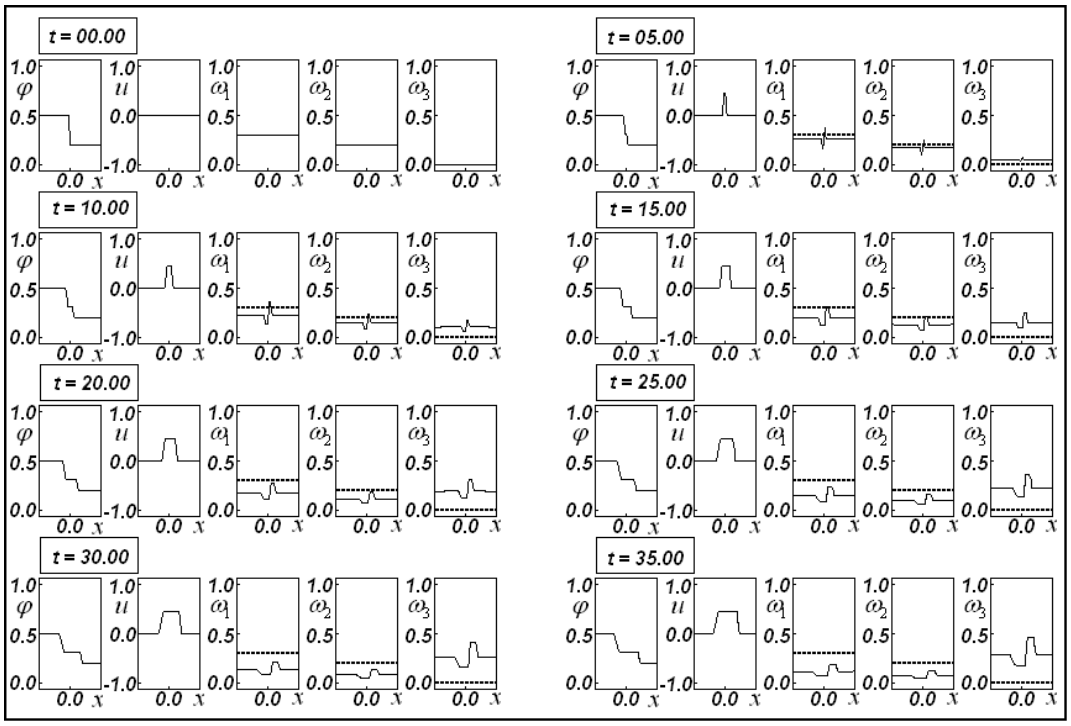

Figure 3. Evolution of saturation φ, velocity u, and the pollutants' concentrations $(\omega_1, \omega_2, \omega_3)$ for $\alpha = \beta = 0.05$ and $\gamma_1 = \gamma_2 = 0.0$.

Figure 4 used the same initial data as in Figure 3, as well as the same concentration coefficients ω_1 and ω_2 ($\alpha = \beta = 0.05$). However, positive drag coefficients were considered for both the linear (Darcy) and quadratic (Forchheimer) terms, with coefficients $\gamma_1 = \gamma_2 = 1.0$.

Comparing Figures 3 and 4, the strong influence of this positive drag is evident. It should be noted that it is a very high-drag situation ($\gamma_1 = \gamma_2 = 1.0$) combined with a high pollutants' reaction rate ($\alpha = \beta = 0.05$). The drag influence, particularly on the pollutants' concentrations, is much stronger than in Figures 1 and 2.

Figure 5 considers the same initial data previously employed in Figures 3 and 4, as well as the same concentration coefficients ω_1 and ω_2 ($\alpha = \beta = 0.05$), but an enormous value for the positive drag term: ($\gamma_1 = \gamma_2 = 5.0$), which is five times greater than the value used in Figure 4.

The radical influence of this drag term on the distributions of all variables underscores the robustness of the numerical methodology employed in this work. The influence on the fluid constituent velocity is enormous.

The drag has a certain "damping" effect on the distributions of all variables.

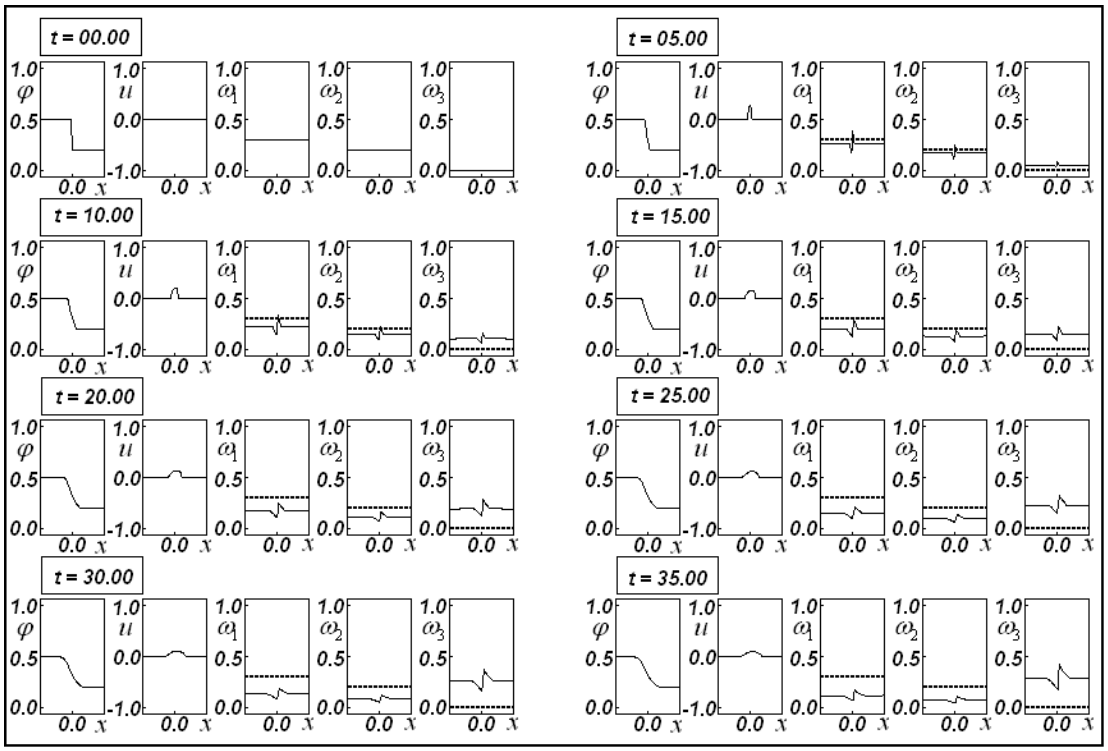

Figure 4. Evolution of saturation φ, velocity u, and the pollutants' concentrations $(\omega_1, \omega_2, \omega_3)$ for $\alpha = \beta = 0.05$ and $\gamma_1 = \gamma_2 = 1.0$.

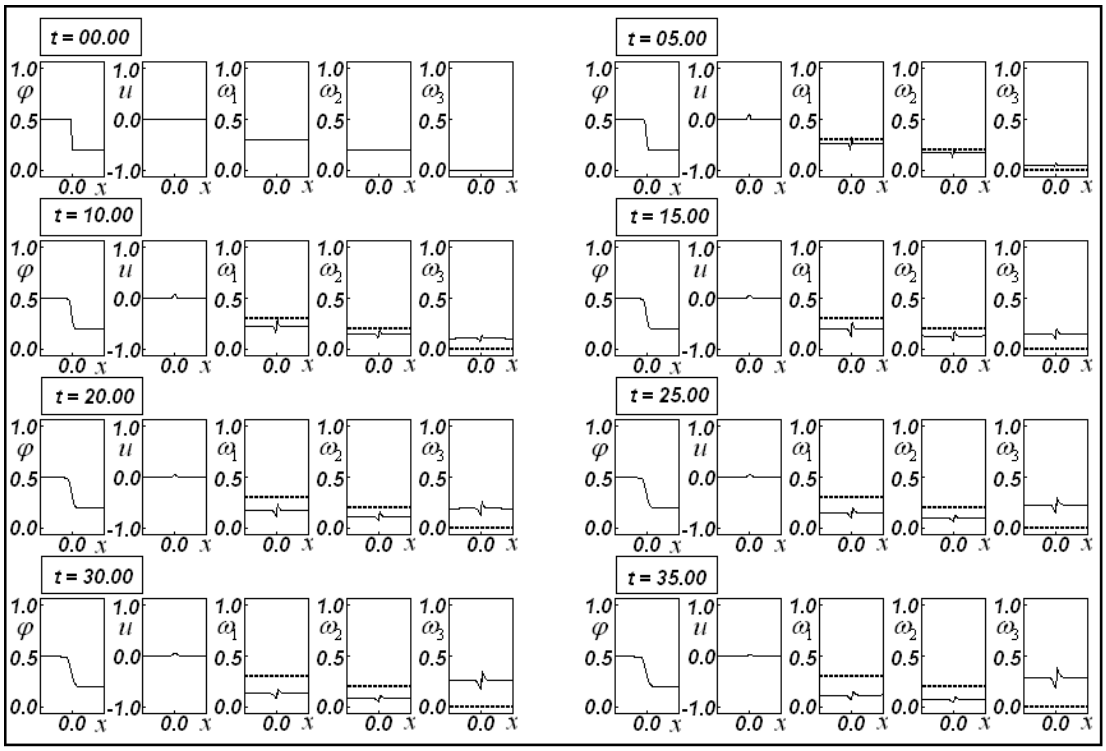

Figure 5. Evolution of saturation φ, velocity u, and the pollutants' concentrations $(\omega_1, \omega_2, \omega_3)$ for $\alpha = \beta = 0.05$ and $\gamma_1 = \gamma_2 = 5.0$.

Figures 6–18 consider initial constant pollutants' concentrations with $\omega_1 = 0.3$, $\omega_2 = 0.2$, and $\omega_3 = 0$. Also, the coefficient of the pollutants' mass generation term is $\alpha = \beta = 0.05$, in all cases. The initial value for the fluid constituent velocity is given by a jump function obeying: $u = +1.0$ for $x < -0.5$, $u = 0.0$ for $-0.5 < x < +0.5$, and $u = -1.0$ for $x > +0.5$. The black dotted lines, associated with the three pollutants, indicate the initial conditions to facilitate easier comparison of the pollutants' concentration evolution over time (for Figures 6–13). The red dotted lines in the saturation graphs indicate the maximum saturation value ($\varphi_{MAX} = 1.0$), which is never exceeded.

Figure 6 presents the evolution of saturation φ, fluid constituent velocity u, and the pollutants' concentrations ω_1, ω_2, and ω_3, and neglecting both viscous drag terms, so that $\gamma_1 = \gamma_2 = 0.0$. The initial condition, illustrated in the first five diagrams on the upper left, assumes a constant saturation ($\varphi = 0.6$) and step functions for the fluid constituent velocity.

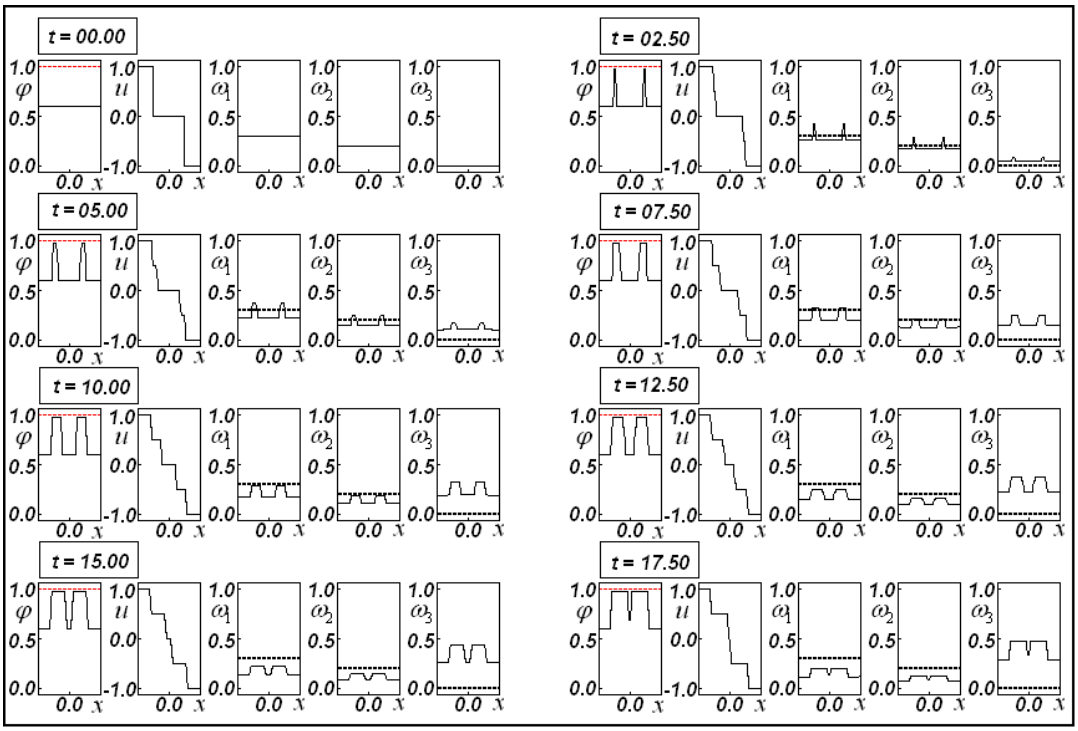

Figure 6. Evolution of saturation φ, velocity u, and the pollutants' concentrations $(\omega_1, \omega_2, \omega_3)$ for $\alpha = \beta = 0.05$ and $\gamma_1 = \gamma_2 = 0.0$, with step functions for the initial velocity.

Figure 7 presents the evolution of saturation φ, fluid constituent velocity u, and the pollutants' concentrations ω_1, ω_2, and ω_3, with the same initial conditions used to obtain Figure 6, but accounting for both linear (Darcy) and quadratic (Forchheimer) drag terms with the positive values $\gamma_1 = \gamma_2 = 0.5$.

Figure 8 presents the evolution of saturation φ, fluid constituent velocity u, and the pollutants' concentrations ω_1, ω_2, and ω_3, for $\alpha = \beta = 0.05$ and neglecting drag terms with $\gamma_1 = \gamma_2 = 0.0$, considering as initial data distinct step functions for saturation (with $\varphi = 0.9$ for $x < -0.5$, $\varphi = 0.6$ for $-0.5 < x < +0.5$, and $\varphi = 0.3$ for $x > +0.5$) and fluid constituent velocity. The results indicate that the saturation reaches the limit value, $\varphi_{MAX} = 1.0$, at all considered time steps (except for the initial condition), as illustrated by the red dotted line.

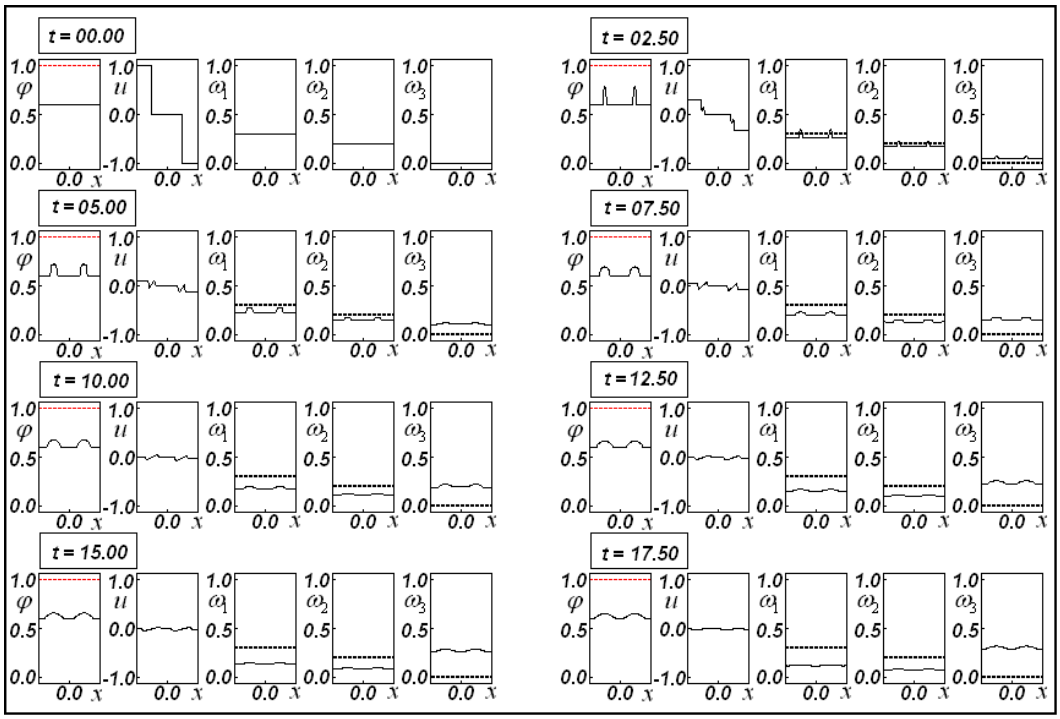

Figure 7. Evolution of saturation φ, velocity u, and the pollutants' concentrations $(\omega_1, \omega_2, \omega_3)$ for $\alpha = \beta = 0.05$ and $\gamma_1 = \gamma_2 = 0.5$, with step functions for the initial velocity.

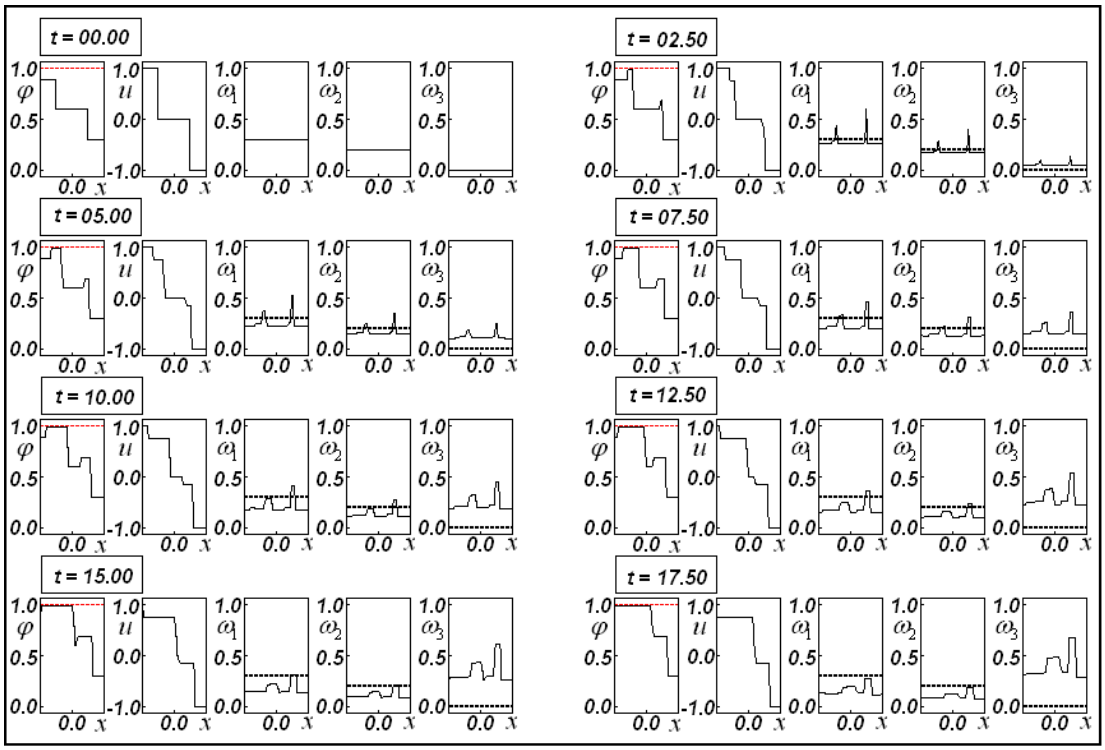

Figure 8. Evolution of saturation φ, velocity u, and the pollutants' concentrations $(\omega_1, \omega_2, \omega_3)$ for $\alpha = \beta = 0.05$ and $\gamma_1 = \gamma_2 = 0.0$, with distinct step functions for the initial saturation and velocity.

Figure 9 uses the same initial data as in Figure 8, but accounts for Darcy and Forchheimer viscous drag terms by using the same coefficients used in Figure 7. It can be noted that the dissipation provoked by the drag terms does not allow the dissipation to reach its maximum value at any time instant. The saturation never reaches the red dotted line. Comparing Figures 8 and 9, it can be observed that the drag terms induce a certain dumping effect.

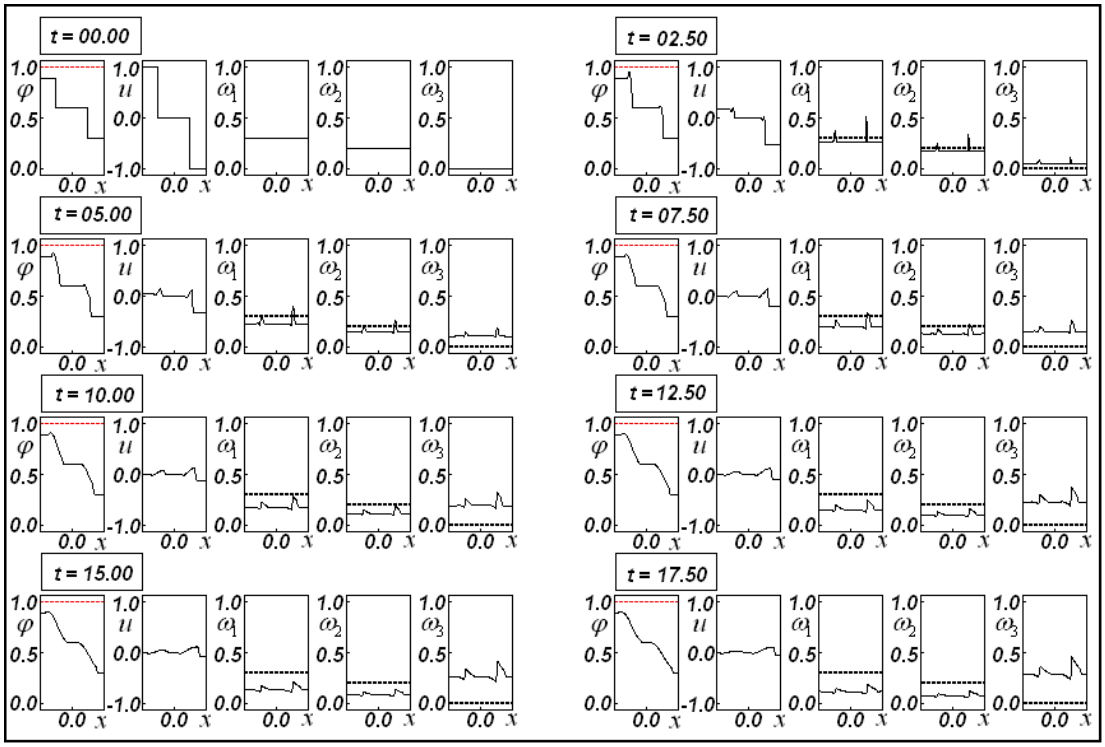

Figure 9. Evolution of saturation φ, velocity u, and the pollutants' concentrations $(\omega_1, \omega_2, \omega_3)$ for $\alpha = \beta = 0.05$ and $\gamma_1 = \gamma_2 = 0.5$, with distinct step functions for the initial saturation and velocity.

Figure 10 presents the evolution of saturation, fluid constituent velocity, and the concentrations of three pollutants, for $\alpha = \beta = 0.05$, neglecting both viscous drag terms, with $\gamma_1 = \gamma_2 = 0.0$. The initial data consider distinct step functions for saturation (with $\varphi = 0.9$ for $x < 0$ and $\varphi = 0.3$ for $x > 0$) and for the fluid constituent velocity. The behavior is analogous to that observed in Figure 8, where, when viscous drag is neglected, the maximum saturation is reached along the saturation evolution. All curves (except for the initial datum) reach the value $\varphi_{MAX} = 1.0$ during the saturation progression.

Figure 11 is obtained using the same initial data as Figure 10, but it accounts for linear and quadratic drag coefficients $\gamma_1 = \gamma_2 = 1.0$. Note that this positive coefficient is twice that used in Figure 9, accentuating the viscous dissipation due to the drag terms. Nonetheless, the saturation reaches its maximum value (given by $\varphi_{MAX} = 1.0$) at the time $t = 2.50$, the second depicted time instant, just after the initial data. As expected, there is a fierce dissipation in the fluid constituent velocity u and in the pollutants' concentrations ω_1, ω_2, and ω_3.

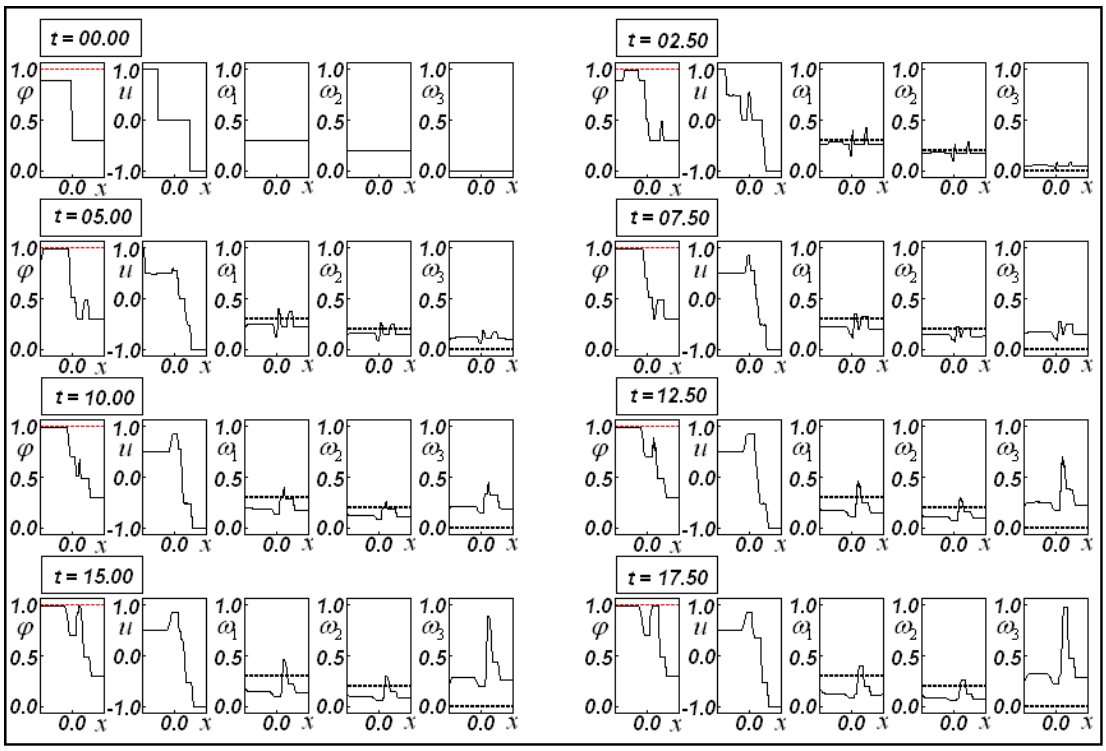

Figure 10. Evolution of saturation φ, velocity u, and the pollutants' concentrations $(\omega_1, \omega_2, \omega_3)$ for $\alpha = \beta = 0.05$ and $\gamma_1 = \gamma_2 = 0.0$, with distinct step functions for the initial saturation and velocity.

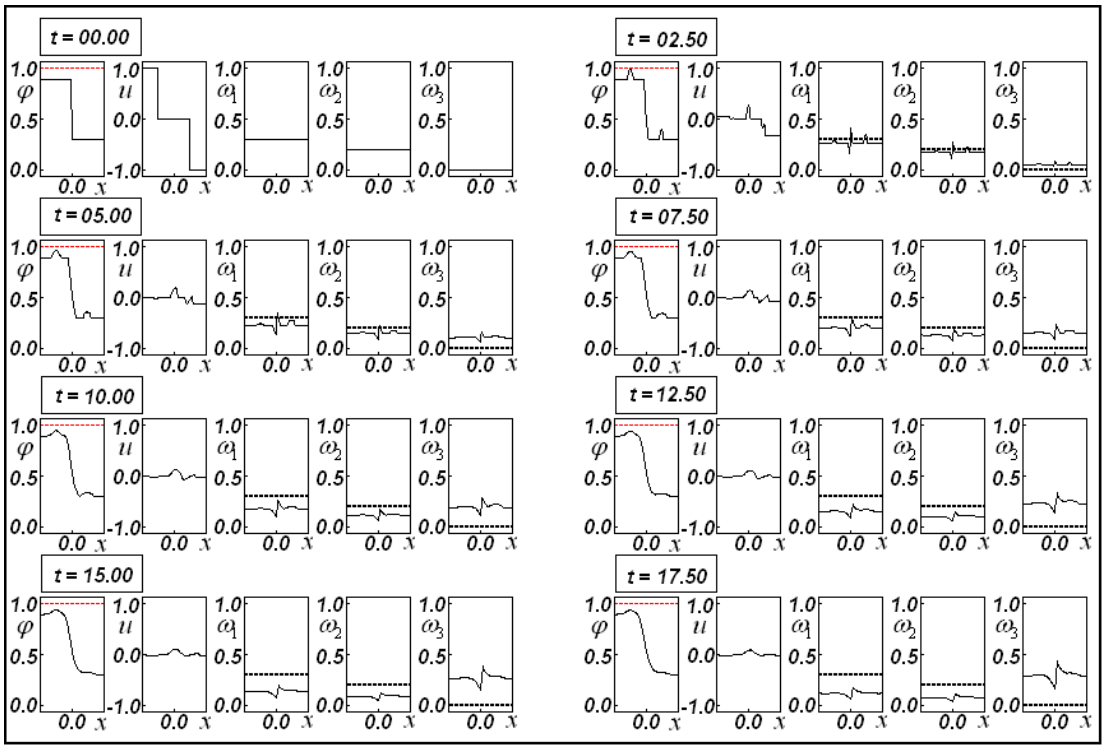

Figure 11. Evolution of saturation φ, velocity u, and the pollutants' concentrations $(\omega_1, \omega_2, \omega_3)$ for $\alpha = \beta = 0.05$ and $\gamma_1 = \gamma_2 = 1.0$, with distinct step functions for the initial saturation and velocity.

Figure 12 exhibits the evolution of saturation φ, fluid constituent velocity u, and the pollutants' concentrations ω_1, ω_2, and ω_3, and neglecting Darcy and Forchheimer drag terms $\gamma_1 = \gamma_2 = 0.0$. The initial data considers the same step function for velocity, but there is an initial jump for the saturation ($\varphi = 0.3$ for $x < -0.5$, $\varphi = 0.9$ for $-0.5 < x < +0.5$, and $\varphi = 0.3$ for $x > +0.5$). In this case, even neglecting the friction (drag), the saturation never reaches the red dotted line ($\varphi_{MAX} = 1.0$).

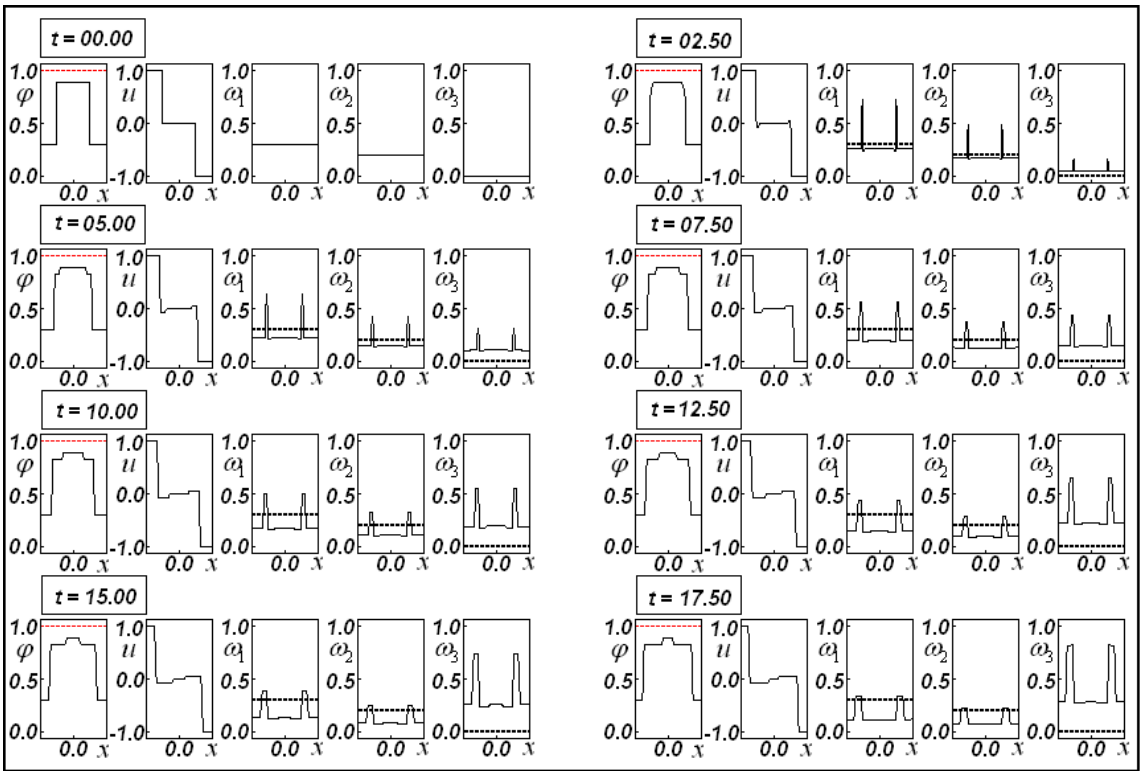

Figure 12. Evolution of saturation φ, velocity u, and the pollutants' concentrations $(\omega_1, \omega_2, \omega_3)$ for $\alpha = \beta = 0.05$ and $\gamma_1 = \gamma_2 = 0.0$, with step functions for the initial velocity and an initial jump for the saturation.

Figure 13 exhibits the evolution of saturation φ, fluid constituent velocity u, and the pollutants' concentrations ω_1, ω_2, and ω_3, accounting for Darcy and Forchheimer drag-term coefficients $\gamma_1 = \gamma_2 = 1.0$. The initial data is the same as that employed in Figure 12. Comparing Figures 12 and 13, the meaningful influence of linear and quadratic drag is evident. It can be easily observed in Figure 14, with Figures 12 and 13 superposed.

Figure 15 depicts the evolution of saturation φ, velocity u, and the pollutants' concentrations ω_1, ω_2, and ω_3, for $\alpha = \beta = 0.05$, with the same step functions for initial velocity considered from Figure 9 on and an initial jump for the saturation ($\varphi = 0.4$ for $x < -0.5$, $\varphi = 0.9$ for $-0.5 < x < +0.5$, and $\varphi = 0.4$ for $x > +0.5$). Note that this initial jump is not exactly the same as that employed in Figures 12 and 13. Although the Darcy and Forchheimer friction factors are neglected, the red dotted line ($\varphi_{MAX} = 1.0$) is never attained.

Figure 16 uses the same initial conditions employed in Figure 15, but accounts for linear (Darcy) and quadratic (Forchheimer) drag terms. The presence of friction allows observation of dissipation throughout the evolution of all variables.

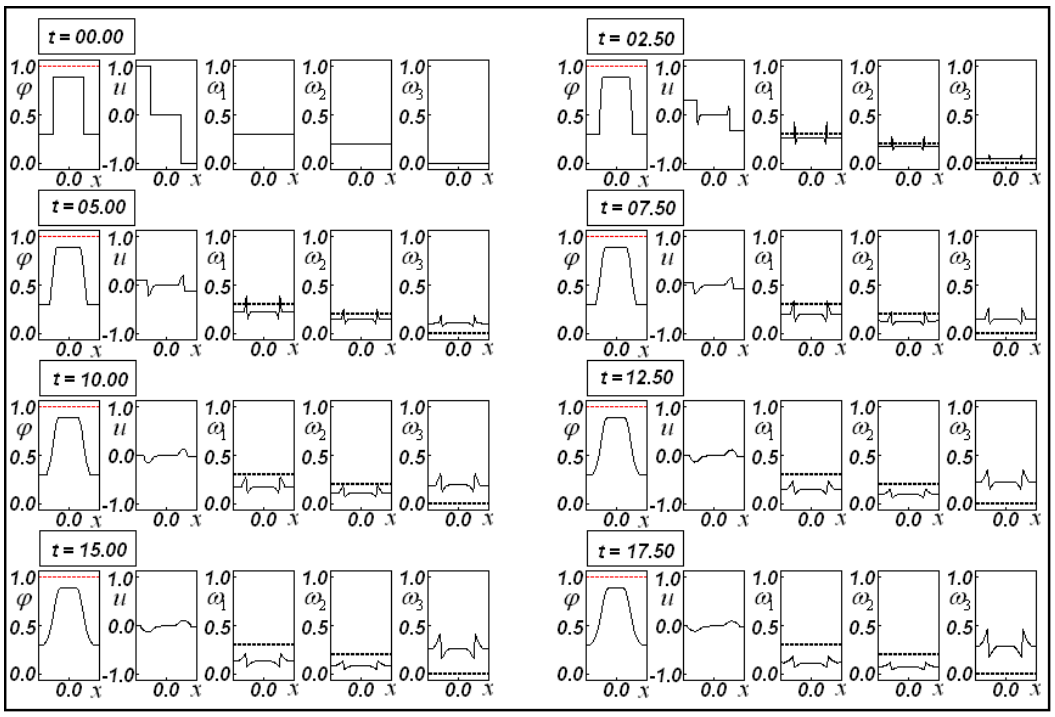

Figure 13. Evolution of saturation φ, velocity u, and the pollutants' concentrations $(\omega_1, \omega_2, \omega_3)$ for $\alpha = \beta = 0.05$ and $\gamma_1 = \gamma_2 = 1.0$, with step functions for the initial velocity and an initial jump for the saturation.

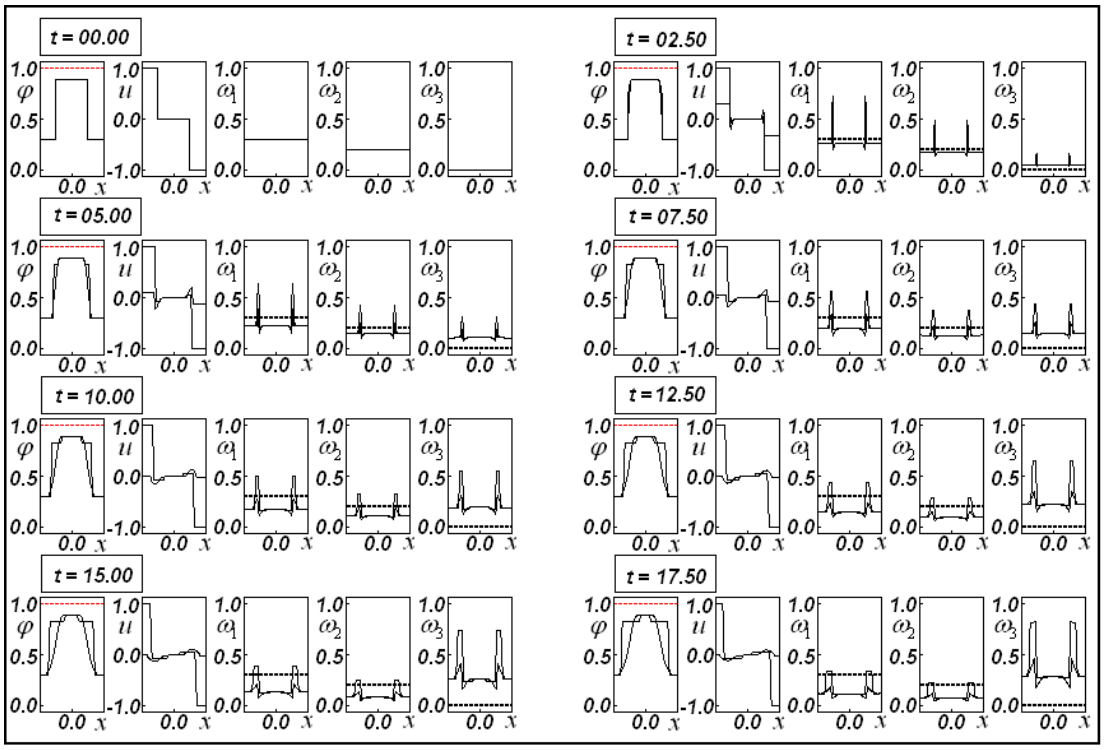

Figure 14. Superposition of Figures 12 $(\gamma_1 = \gamma_2 = 0.0)$ and 13 $(\gamma_1 = \gamma_2 = 1.0)$ to visualize the influence of the viscous drag terms.

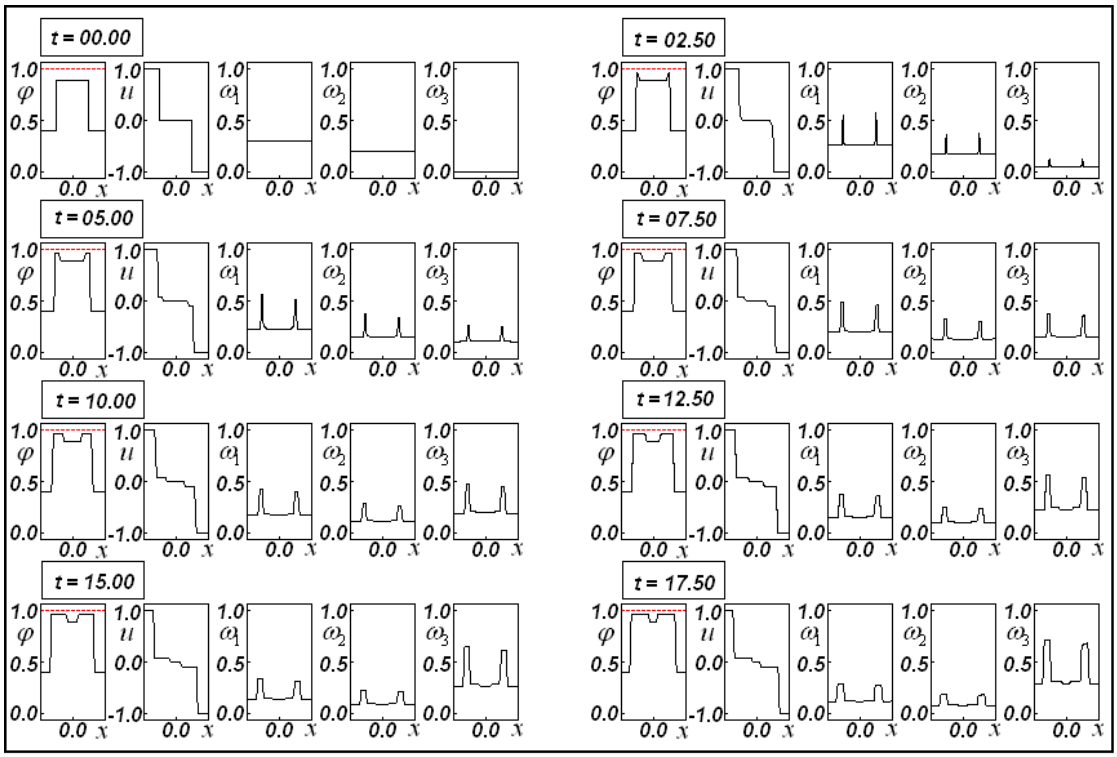

Figure 15. Evolution of saturation φ, velocity u, and the pollutants' concentrations $(\omega_1, \omega_2, \omega_3)$ for $\alpha = \beta = 0.05$ and $\gamma_1 = \gamma_2 = 0.0$, with step functions for the initial velocity and an initial jump for the saturation.

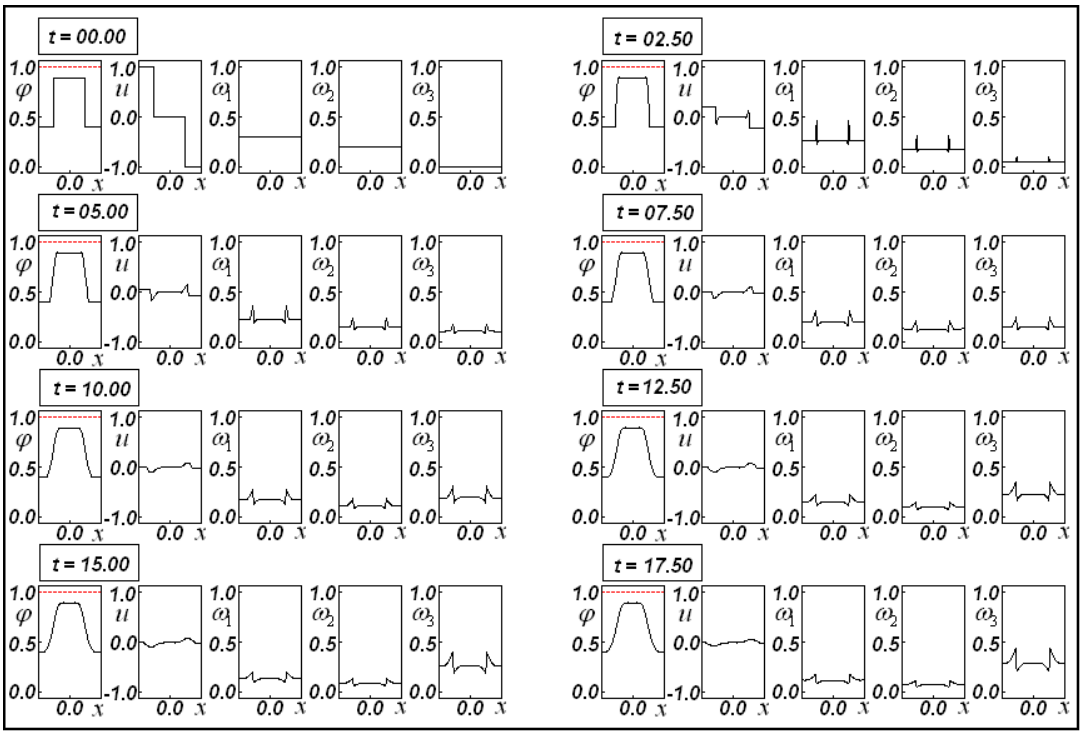

Figure 16. Evolution of saturation φ, velocity u, and the pollutants' concentrations $(\omega_1, \omega_2, \omega_3)$ for $\alpha = \beta = 0.05$ and $\gamma_1 = \gamma_2 = 1.0$, with step functions for the initial velocity and an initial jump for the saturation.

Figure 17 is analogous to Figure 16, with the same initial conditions, $\alpha = \beta = 0.05$, but the drag terms are five times greater than those in Figure 16, with very large drag coefficients: $\gamma_1 = \gamma_2 = 5.0$.

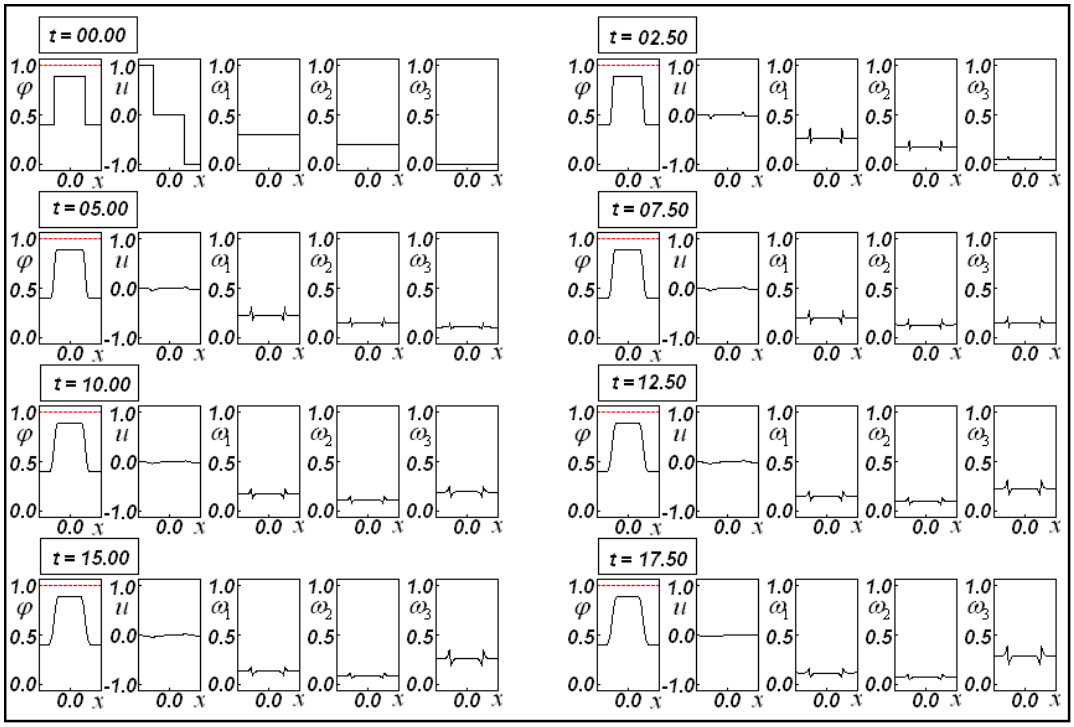

Figure 17. Evolution of saturation φ, velocity u, and the pollutants' concentrations $(\omega_1, \omega_2, \omega_3)$ for $\alpha = \beta = 0.05$ and $\gamma_1 = \gamma_2 = 5.0$, with step functions for the initial velocity and an initial jump for the saturation.

Comparing Figures 15–17, it can be noted that such a high friction term as the one used in Figure 17 led to almost stagnant velocities. Moreover, very low velocities have a small influence on the behavior of the pollutant constituents.

Figure 18 considers a distinct jump in saturation ($\varphi = 0.4$ for $x < -0.5$, $\varphi = 0.95$ for $-0.5 < x < +0.5$, and $\varphi = 0.4$ for $x > +0.5$), the same step function for the velocity, and $\alpha = \beta = 0.05$. The drag terms are neglected ($\gamma_1 = \gamma_2 = 0.0$). In this case, the jump in the initial condition reaches a higher value, and the maximal admissible saturation, given by the red dotted line, is attained for all considered time steps after the initial data, in this case, without Darcy and Forchheimer drag.

Figure 19 employs the same initial data used in Figure 18, but includes the linear and quadratic drag terms, given by $\gamma_1 = \gamma_2 = 1.0$. Comparing Figures 18 and 19, the dissipation along with the evolution of all considered variables can be observed.

The mechanical response of the main fluid deserves a separate special remark. When the velocities decrease as x increases, there is a tendency for an increasing saturation, since the fluid is being "compressed" and, therefore, a pressure increase is observed. On the other hand, if the velocities increase as x increases, the tendency is a decrease in pressure and, consequently, in saturation. This behavior is easily observed in figures showing a velocity jump. However, this effect becomes less evident when there are drag forces ($\gamma_1 \neq 0.0$ or $\gamma_2 \neq 0.0$), since these drag forces play the role of a momentum sink.

It is also remarkable that saturation jumps lead to severe alterations in motion. The cases in which the initial velocity is zero everywhere allow us to observe, explicitly, the saturation jump originating a motion.

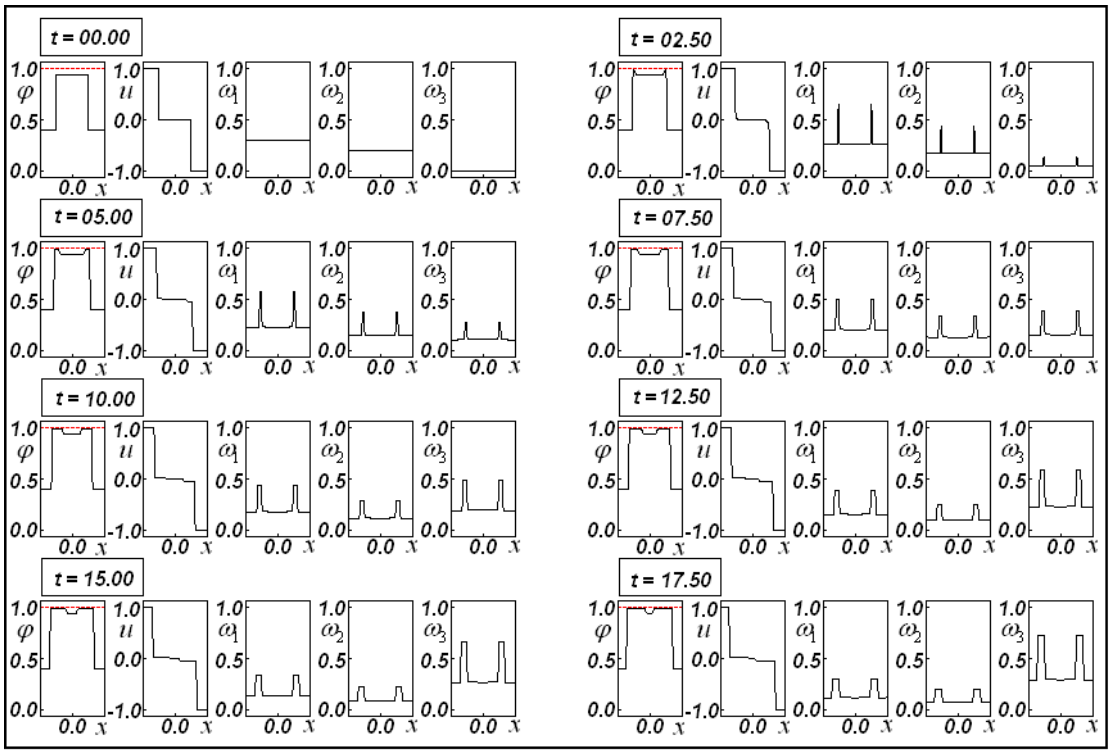

Figure 18. Evolution of saturation φ, velocity u, and the pollutants' concentrations $(\omega_1, \omega_2, \omega_3)$ for $\alpha = \beta = 0.05$ and $\gamma_1 = \gamma_2 = 0.0$, with step functions for the initial velocity and an initial jump for the saturation.

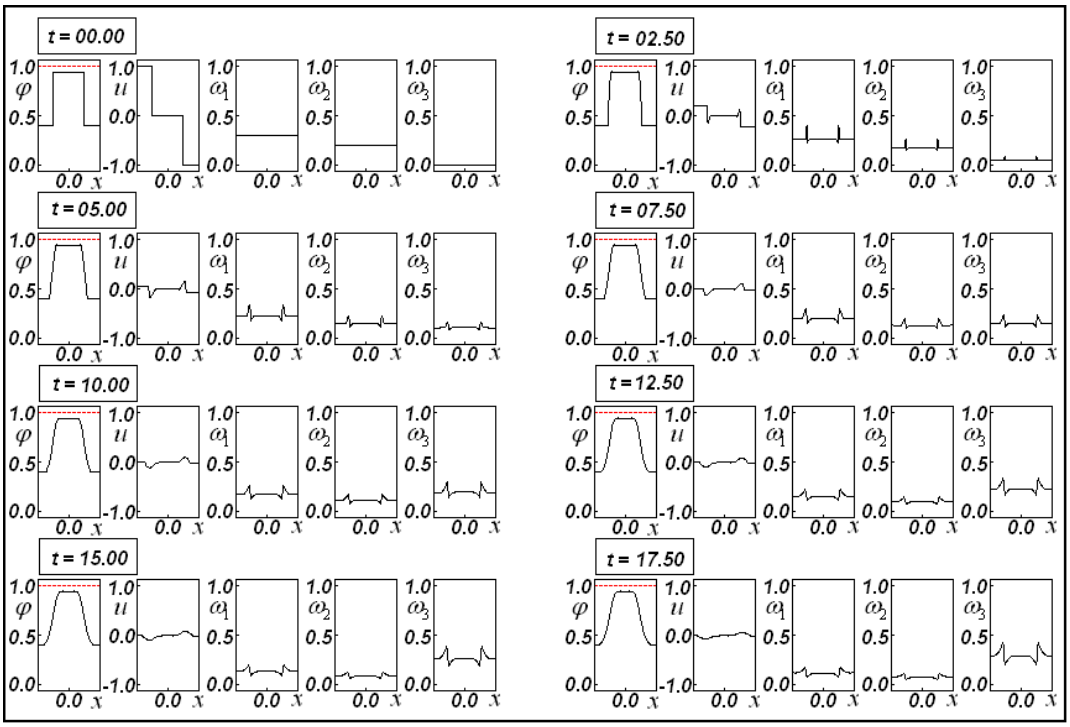

Figure 19. Evolution of saturation φ, velocity u, and the pollutants' concentrations $(\omega_1, \omega_2, \omega_3)$ for $\alpha = \beta = 0.05$ and $\gamma_1 = \gamma_2 = 1.0$, with step functions for the initial velocity and an initial jump for the saturation.

It is important to highlight the strong dependence of concentrations on saturation results. A small variation in saturation can lead to significant increases or decreases in the concentrations of all pollutant constituents. There is also an indirect influence on the velocity distribution, since velocities affect concentrations and concentrations affect velocities. This effect could be partially justified by the behavior of the Riemann invariants. From the definition of the i-th pollutant concentration in the mixture ω_i, presented in Eq (2.1), this strong dependence would be expected.

5. Conclusions

This work used a mixture theory approach to simulate a nonlinear, non-homogeneous hyperbolic system that represents constrained flows containing suspended pollutants through porous media. The pollutants react chemically with one another, giving rise to a mass generation rate term for each pollutant mass balance. In addition to chemical reactions among the pollutant constituents, linear and quadratic drag terms (usually called Darcy and Forchheimer terms) are present in the momentum source term (for the fluid constituent). The influence of these two drag terms is very relevant in real engineering problems, specifically in this case, when the fluid flowing through the porous matrix can be viewed as a pseudo-mixture of a (main) fluid constituent and N pollutant constituents.

The numerical simulation used a variant of the Glimm method that accounts for the influence of the sign of the random number, considering four completely independent evolutions, each of them with its own randomly chosen number, making an average of four evolutions to reach the result of the Glimm scheme for a given time step, giving rise to more accurate positions for shocks and rarefaction waves. The Glimm method marches in time using a previously chosen number of Riemann problems. Once this approximation is reached, the same time step is used to implement an operator-splitting procedure. So, the Glimm scheme was combined with an operator-splitting scheme to solve the non-homogeneous system.

The constitutive relation for pressure as a function of the saturation allows a tiny, controlled supersaturation. Besides, it allows one to obtain an explicit closed-form expression for the Riemann invariants. The complete (exact) solution for the associated Riemann problem is presented in the Appendix. The combination of the Glimm method with an operator-splitting technique is a reliable tool for describing the transition from unsaturated to saturated flow (and vice versa) using the same numerical methodology. This tool preserves the problem's hyperbolic nature, ensuring physically consistent results (see [20]). The influence of linear and quadratic drag terms is clearly evident in all variables (saturation, fluid constituent velocity, and concentrations of three pollutants) for the simulated polluted flow through a porous matrix.

Finally, we would like to emphasize that we have proposed a new constitutive relation embedding a kinematical constraint (so that the saturation meaning was preserved without losing the hyperbolic structure), we have accounted for both linear and nonlinear drag terms in the interaction force (in addition to the advective term, mandatory for unsaturated flows), and we have accounted for chemical interactions among the pollutant constituents, using a simple constitutive assumption. We have also employed a new protocol for the Glimm scheme, using four random choices at each time step, thereby increasing the precision already ensured by the Glimm scheme for the shock positions.

Regarding future developments of this research, the first step would be to consider more realistic chemical reactions that account for stoichiometry. Subsequently, the restriction to very low pollutant levels could be disregarded, allowing higher concentrations. Next, the problem could be considered in multiple dimensions.

Author contributions

R. M. Saldanha da Gama and M. L. Martins-Costa: Conceptualization, Formal analysis, Writing–original draft; R. M. Saldanha da Gama, H. S. da Costa Mattos and M. L. Martins-Costa: Funding acquisition; R. P. S. Gama, R. M. Saldanha da Gama and F. B. Freitas Rachid: Investigation; R. P. S. Gama and D. A. Monteiro: Methodology; M. L. Martins-Costa and H. S. da Costa Mattos: Project administration, Writing–review and editing; R. P. S. Gama, R. M. Saldanha da Gama and M. L. Martins-Costa: Software; M. L. Martins-Costa, R. M. Saldanha da Gama and F. B. Freitas Rachid: Supervision; R. M. Saldanha da Gama, F. B. Freitas Rachid and D. A. Monteiro: Validation. All authors have read and agreed to the published version of the manuscript.

Use of Generative-AI tools declaration

The authors declare that they have not used Artificial Intelligence (AI) tools in the creation of this article.

Acknowledgments

The authors gratefully thank the Brazilian agency **CNPq** for the financial support.

Conflict of interest

The authors declare no conflicts of interest.

References

1. M. Francaviglia, A. Palumbo, P. Rogolino, Thermodynamics of mixtures as a problem with internal variables. The general theory, *J. Non Equil. Thermody.*, **31** (2006), 419–429. http://dx.doi.org/10.1515/JNETDY.2006.018
2. J. Bear, *Dynamics of fluids in porous media*, New York: Dover Publications, 1988.
3. A. E. Scheidegger, *The physics of flow through porous media*, 3 Eds., University of Toronto Press, 1974.
4. J. Bear, *Hydraulics of groundwater*, Mineola, New York: Dover Publications, 1979.
5. M. Kaviany, *Principles of heat transfer in porous media*, 2 Eds.; New York: Springer, 1995. https://doi.org/10.1007/978-1-4612-4254-3
6. E. Holzbecher, Reactive transport in porous media–concepts and numerical approaches, In: *Transport phenomena in porous media III*, Elsevier, 2005, 305–340. https://doi.org/10.1016/B978-008044490-1/50016-8
7. L. Ma, D. B. Ingham, M. C. Pourkashanian, Application of fluid flows through porous media in fuel cells, In: *Transport phenomena in porous media III*, Elsevier, 2005, 418–440. https://doi.org/10.1016/B978-008044490-1/50020-X
8. X. Shu, Y. Q. Wu, X. Zhang, F. Yu, Experiments and models for contaminant transport in unsaturated and saturated porous media–a review, *Chem. Eng. Res. Design*, **192** (2023), 606–621. https://doi.org/10.1016/j.cherd.2023.02.022

9. R. J. Atkin, R. E. Craine, Continuum theories of mixtures: basic theory and historical development, *Q. J. Mech. Appl. Math.*, **29** (1976), 209–244. https://doi.org/10.1093/qjmam/29.2.209
10. R. M. Bowen, Compressible porous media models by use of the theory of mixtures, *Int. J. Eng. Sci.*, **20** (1982), 697–735. https://doi.org/10.1016/0020-7225(82)90082-9
11. A. Bedford, D. S. Drumheller, Theories of immiscible and structured mixtures, *Int. J. Eng. Sci.*, **21** (1983), 863–960. https://doi.org/10.1016/0020-7225(83)90071-X
12. K. R. Rajagopal, L. Tao, *Mechanics of mixtures*, Singapore: World Scientific, 1995. https://doi.org/10.1142/2197
13. B. D. Coleman, W. Noll, The thermodynamics of elastic materials with heat conduction and viscosity, *Arch. Ration. Mech. Anal.*, **13** (1963), 168–178. https://doi.org/10.1007/BF01262690
14. H. S. da Costa Mattos, M. L. Martins-Costa, R. M. S. da Gama, On the modeling of momentum and energy transfer in incompressible mixtures, *Int. J. Non Linear Mech.*, **30** (1995), 419–431. https://doi.org/10.1016/0020-7462(95)00016-H
15. M. L. Martins-Costa, R. M. S. da Gama, Constitutive relations for the energy transfer in nonsaturated continuous mixtures, *Mech. Res. Commun.*, **23** (1996), 117–122. https://doi.org/10.1016/0093-6413(96)00002-X
16. M. L. Martins-Costa, R. M. S. da Gama, A mixture theory model for the forced convection flow through an unsaturated wellbore, *Int. J. Heat Fluid Flow*, **26** (2005), 141–155. https://doi.org/10.1016/j.ijheatfluidflow.2004.06.003
17. S. I. Abdelsalam, M. Khairy, W. Abbas, A. M. Megahed, M. S. Emam, Semi analytical solution of MHD and heat transfer of couple stress fluid over a stretching sheet with radiation in porous medium, *Front. Heat Mass Transfer*, **23** (2025), 1833–1846. https://doi.org/10.32604/fhmt.2025.069711
18. M. M. Bhatti, H. F. Oztop, R. Ellahi, F. Z. Duraihem, Numerical analysis of Maxwell fluid flow with quadratic convection under inclined magnetic field employing Lie symmetry and Chebyshev spectral techniques, *Int. J. Numer. Methods Heat Fluid Flow*, **36** (2026), 1140–1169. https://doi.org/10.1108/HFF-09-2025-0682
19. M. M. Bhatti, R. Ellahi, S. M. Sait, Numerical investigation of magnetized nanofluid flow in a non-Darcian medium with convective heating conditions across a rotating disk, *Int. J. Numer. Methods Heat Fluid Flow*, **35** (2025), 1736–1763. https://doi.org/10.1108/HFF-03-2025-0135
20. R. M. S. da Gama, J. J. P. Filho, R. P. S. da Gama, D. C. da Silva, C. H. Alexandrino, M. L. Martins-Costa, Numerical simulation of constrained flows through porous media employing Glimm's scheme, *Axioms*, **12** (2023), 1023. https://doi.org/10.3390/axioms12111023
21. M. L. Martins-Costa, F. B. de Freitas Rachid, R. P. S. da Gama, R. M. S. da Gama, Combining Glimm's scheme and operator splitting for simulating constrained flows in porous media, *Axioms*, **13** (2024), 587. https://doi.org/10.3390/axioms13090587
22. W. O. Williams, Constitutive equations for flow of an incompressible viscous fluid through a porous medium, *Q. Appl. Math.*, **36** (1978), 255–267.
23. M. B. Allen, Mechanics of multiphase fluid flows in variably saturated porous media, *Int. J. Eng. Sci.*, **24** (1986), 339–351. https://doi.org/10.1016/0020-7225(86)90090-X
24. S. Srinivasan, K. R. Rajagopal, A thermodynamic basis for the derivation of the Darcy, Forchheimer and Brinkman models for flows through porous media and their generalizations, *Int. J. Non Linear Mech.*, **58** (2014), 162–166. https://doi.org/10.1016/j.ijnonlinmec.2013.09.004

25. D. A. Nield, The limitations of the Brinkmann-Forchheimer equations in modeling flow in a saturated porous medium and at the interface, *Int. J. Heat Fluid Flow*, **12** (1991), 269–272. https://doi.org/10.1016/0142-727X(91)90062-Z
26. R. M. S. da Gama, M. L. Martins-Costa, Incompressible fluid flow and heat transfer through a nonsaturated porous medium, *Comput. Mech.*, **20** (1997), 479–494. https://doi.org/10.1007/s004660050269
27. M. L. Martins-Costa, R. M. S. da Gama, Numerical simulation of one-dimensional flows through porous media with shock waves, *Int. J. Numer. Methods Eng.*, **52** (2001), 1047–1067. https://doi.org/10.1002/nme.233
28. J. Glimm, Solutions in the large for nonlinear hyperbolic systems of equations, *Commun. Pure Appl. Math*., **18** (1965), 697–715. https://doi.org/10.1002/cpa.3160180408
29. A. J. Chorin, Random choice solution of hyperbolic systems, *J. Comput. Phys.*, **22** (1976), 517–533. https://doi.org/10.1016/0021-9991(76)90047-4
30. J. Smoller, *Shock-waves and reaction-diffusion equations*, New York: Springer, 1994. https://doi.org/10.1007/978-1-4612-0873-0
31. H. Olivier, H. Grönig, The random choice method applied to two-dimensional shock focusing and diffraction, *J. Comput. Phys.*, **63** (1986), 85–106. https://doi.org/10.1016/0021-9991(86)90085-9
32. E. Godlewski, P. A. Raviart, *Numerical approximation of hyperbolic systems of conservation laws*, New York: Springer, 2021. https://doi.org/10.1007/978-1-0716-1344-3
33. E. F. Toro, *Riemann solvers and numerical methods for fluid dynamics*, Berlin, Heidelberg: Springer, 2009. https://doi.org/10.1007/b79761
34. C. M. Dafermos, *Hyperbolic conservation laws in continuum physics*, Berlin, Heidelberg: Springer, 2016. https://doi.org/10.1007/978-3-662-49451-6
35. P. Lax, Shock waves and entropy, In: *Contributions to nonlinear functional analysis*, Academic Press, 1971. https://doi.org/10.1016/B978-0-12-775850-3.50018-2
36. B. L. Keyfitz, H. C. Kranzer, Existence and uniqueness of entropy solutions to the Riemann problem for hyperbolic systems of two nonlinear conservation laws, *J. Differ. Equ.*, **27** (1978), 444–476. https://doi.org/10.1016/0022-0396(78)90062-1

Appendix

Associated Riemann problem

The homogeneous portion of Eq (2.7) may be conveniently expressed as

$$\frac{\partial}{\partial t}\begin{bmatrix}\varphi\\ \varphi u\\ \omega_i\end{bmatrix}+\mathbf{A}\frac{\partial}{\partial x}\begin{bmatrix}\varphi\\ \varphi u\\ \omega_i\end{bmatrix}=0,\quad \mathbf{A}=\begin{bmatrix}0 & 1 & 0\\ p'-u^2 & 2u & 0\\ -\omega_i u/\varphi & \omega_i/\varphi & u\end{bmatrix},\quad i=1,n,\ \text{with}\ p'=\frac{\varphi^2}{(1-\varphi)^4}, \tag{A.1}$$

and the Cauchy problem is such that

$$\begin{aligned}
&\frac{\partial \varphi}{\partial t}+\frac{\partial}{\partial x}(\varphi u)=0, \quad \frac{\partial}{\partial t}(\varphi u)+\frac{\partial}{\partial x}\left(\varphi u^2+\frac{\varphi^3}{3(1-\varphi)^3}\right)=0,\\
&\frac{\partial \omega_i}{\partial t}+\frac{\partial}{\partial x}(\omega_i u)=0,\\
&(\varphi,u,\omega_i)=\begin{cases}(\varphi_L,u_L,\omega_{iL}), & -\infty<x<0, \quad t=0,\\ (\varphi_R,u_R,\omega_{iR}), & 0<x<\infty, \quad t=0,\end{cases} \qquad i=1,n.
\end{aligned} \tag{A.2}$$

Problem (A.2) is a Riemann problem, and its solution (in a generalized sense) depends solely on the ratio x/t. Using the similarity variable $\eta = x/t$, the homogeneous portion of Eq (2.7) may be represented as

$$\begin{bmatrix} -x/t & 1 & 0 \\ \dfrac{\varphi^2}{(1-\varphi)^4}-u^2 & 2u-x/t & 0 \\ -u\omega_i/\varphi & \omega_i/\varphi & u-x/t \end{bmatrix} \begin{bmatrix} d\varphi \\ d(\varphi u) \\ d\omega_i \end{bmatrix} = \begin{bmatrix} 0 \\ 0 \\ 0 \end{bmatrix}. \tag{A.3}$$

To satisfy Eq (A.3), either φ, u, and ω_i are constant or $\eta = \lambda$, with λ being the eigenvalue of $\mathbf{A}$ and $(d\varphi, d(\varphi u), d\omega_i)^T$ being the eigenvector of $\mathbf{A}$. The eigenvalues of the matrix $\mathbf{A}$ in increasing order are given by

$$\lambda_1 = u-\frac{\varphi}{(1-\varphi)^2}, \quad \lambda_2 = u, \quad \text{and} \quad \lambda_3 = u+\frac{\varphi}{(1-\varphi)^2}. \tag{A.4}$$

Note that the eigenvalues λ_1 and λ_3 presented in Eq (A.4) are unbounded. This is essential for ensuring the unilateral constraint $\lim_{\varphi\to 1} p = +\infty$, presented in Eq (2.9).

The eigenvectors are obtained by substituting for λ_i the ratio x/t in Eq (A.3), so that

$$\text{Associated with } \lambda_1 \begin{cases} \displaystyle\int \frac{1}{(1-\varphi)^2}d\varphi + u = \text{constant and } \frac{\omega_i}{\varphi} = \text{constant}, \\ \text{or} \quad \displaystyle\left(\int \frac{1}{(1-\varphi)^2}d\varphi + \frac{\varphi}{(1-\varphi)^2}\right) + \lambda_1 = \text{constant}, \\ \Rightarrow \quad \displaystyle\frac{1}{(1-\varphi)^2} + \lambda_1 = \text{constant}, \end{cases} \tag{A.5}$$

$$\text{Associated with } \lambda_2 \begin{cases} u = \text{constant and } \varphi = \text{constant}, \\ \Rightarrow \quad \lambda_2 = \text{constant}, \end{cases} \tag{A.6}$$

$$\text{Associated with } \lambda_3 \begin{cases} -\int \frac{1}{(1-\varphi)^2} d\varphi + u = \text{constant and } \frac{\omega_i}{\varphi} = \text{constant}, \\ \text{or} \quad -\left(\int \frac{1}{(1-\varphi)^2} d\varphi + \frac{\varphi}{(1-\varphi)^2} \right) + \lambda_3 = \text{constant}, \\ \Rightarrow \quad -\frac{1}{(1-\varphi)^2} + \lambda_3 = \text{constant}. \end{cases} \tag{A.7}$$

Note that, due to the eigenvectors expressed in Eq (A.4), $\varphi_{**} = \varphi_*$ and $u_{**} = u_*$.

The functional relation between the pressure and the saturation, φ, stated in Eq (2.9), ensures that $2p' + \varphi p'' > 0$. In consequence, along a 1-rarefaction and along a 3-rarefaction, the saturation is such that

$$\begin{aligned} \varphi &= 1 - \frac{1}{\sqrt{\text{constant} - \eta}} = 1 - \frac{1}{\sqrt{(1-\varphi_L)^{-2} + \lambda_{1L} - \eta}} \to \text{1-rarefaction}, \\ \varphi &= 1 - \sqrt{-\frac{1}{\text{constant} - \eta}} = 1 - \sqrt{\frac{1}{(1-\varphi)^{-2} - \lambda_{3R} + \eta}} \to \text{3-rarefaction}. \end{aligned} \tag{A.8}$$

Since the velocity is constant except for rarefactions 1 and 3 ($\lambda_2 = u = \text{constant}$), there is no 2-rarefaction. If the following relation is verified:

$$u_R - u_L \geq \left| \int_{\varphi_L}^{\varphi_R} \frac{\sqrt{p'}}{\varphi} d\varphi \right| \quad \Leftrightarrow \quad u_R - u_L \geq \left| \frac{1}{(1-\varphi_R)^2} - \frac{1}{(1-\varphi_L)^2} \right|, \tag{A.9}$$

then the solution is 1-rarefaction/2-contact shock/3-rarefaction, given by

$$\varphi = \begin{cases} \varphi_L, & -\infty < \eta \leq \lambda_{1L}, \\ 1 - \left\{ (1-\varphi_L)^{-2} + \lambda_{1L} - \eta \right\}^{-1/2}, & \lambda_{1L} < \eta < \lambda_{1*}, \\ \varphi_*, & \lambda_{1*} \leq \eta \leq \lambda_{3*}, \\ 1 - \left\{ (1-\varphi_R)^{-2} - \lambda_{3R} + \eta \right\}^{-1/2}, & \lambda_{3*} < \eta < \lambda_{3R}, \\ \varphi_R, & \lambda_{3R} \leq \eta < \infty, \end{cases} \tag{A.10}$$

$$u = \begin{cases} u_L, & -\infty < \eta \leq \lambda_{1L}, \\ (1-\varphi_L)^{-1} + u_L - \left\{ (1-\varphi_L)^{-2} + \lambda_{1L} - \eta \right\}^{1/2}, & \lambda_{1L} < \eta < \lambda_{1*}, \\ u_*, & \lambda_{1*} \leq \eta \leq \lambda_{3*}, \\ -(1-\varphi_R)^{-1} + u_R + \left\{ (1-\varphi_R)^{-2} - \lambda_{3R} + \eta \right\}^{1/2}, & \lambda_{3*} < \eta < \lambda_{3R}, \\ u_R, & \lambda_{3R} \leq \eta < \infty, \end{cases} \tag{A.11}$$

$$\omega_i = \begin{cases} \omega_{iL}, & -\infty < \eta \le \lambda_{1L}, \\ \dfrac{\omega_{iL}}{\varphi_L}\left\{1-\left\{\left(1-\varphi_L\right)^{-2}+\lambda_{1L}-\eta\right\}^{-1/2}\right\}, & \lambda_{1L} < \eta < \lambda_{1*}, \\ \dfrac{\omega_{iL}\varphi_*}{\varphi_L}, & \lambda_{1*} \le \eta \le u_*, \\ \dfrac{\omega_{iR}\varphi_*}{\varphi_R}, & u_* \le \eta \le \lambda_{3*}, \\ \dfrac{\omega_{iR}}{\varphi_R}\left\{1-\left\{\left(1-\varphi_R\right)^{-2}-\lambda_{3R}+\eta\right\}^{-1/2}\right\}, & \lambda_{3*} < \eta < \lambda_{3R}, \\ \omega_{iR}, & \lambda_{3R} \le \eta < \infty, \end{cases} \tag{A.12}$$

with

$$\varphi_* = 1-\frac{2}{\left(\dfrac{1}{1-\varphi_L}+\dfrac{1}{1-\varphi_R}+u_L-u_R\right)}, \quad u_* = \frac{u_L+u_R}{2}+\frac{1}{\left(1-\varphi_L\right)^2}-\frac{1}{\left(1-\varphi_R\right)^2}, \tag{A.13}$$

and

$$\lambda_{1L} = u_L-\frac{\varphi_L}{\left(1-\varphi_L\right)^2}, \quad \lambda_{1*} = u_*-\frac{\varphi_*}{\left(1-\varphi_*\right)^2}, \quad \lambda_{3*} = u_*+\frac{\varphi_*}{\left(1-\varphi_*\right)^2}, \quad \text{and} \quad \lambda_{1R} = u_R+\frac{\varphi_R}{\left(1-\varphi_R\right)^2}. \tag{A.14}$$

It should be noted that discontinuous solutions must satisfy the entropy conditions to be called shocks: any two states are connected by a discontinuity if and only if they cannot be connected by a continuous function [32–34]. Also, the Rankine-Hugoniot jump conditions [30,35,36] must be satisfied.

The solution is 1-shock / 2-contact shock / 3-shock when the following relation is verified:

$$u_R-u_L \le -\sqrt{\left(\frac{1}{\varphi_R}-\frac{1}{\varphi_L}\right)\left(\frac{\varphi_L^3}{3\left(1-\varphi_L\right)^3}-\frac{\varphi_R^3}{3\left(1-\varphi_R\right)^3}\right)}. \tag{A.15}$$

This is given by

$$\varphi = \begin{cases} \varphi_L, & -\infty < \eta < s_1, \\ \varphi_*, & s_1 < \eta < s_3, \\ \varphi_R, & s_3 < \eta < \infty, \end{cases} \tag{A.16}$$

$$u = \begin{cases} u_L, & -\infty < \eta < s_1, \\ u_*, & s_1 < \eta < s_3, \\ u_R, & s_3 < \eta < \infty, \end{cases} \tag{A.17}$$

$$\omega_i = \begin{cases} \omega_{iL}, & -\infty < \eta < s_1, \\ \omega_{i*} = \omega_{iL}\dfrac{(u_L - s_1)}{(u_* - s_1)}, & s_1 < \eta < u_*, \\ \omega_{i**} = \omega_{iR}\dfrac{(u_R - s_3)}{(u_* - s_3)}, & u_* < \eta < s_3, \\ \omega_{iR}, & s_3 < \eta < \infty. \end{cases} \tag{A.18}$$

This includes the intermediate values φ_* and u_* obtained from

$$\begin{aligned} u_* - u_L &= -\sqrt{\left(\frac{1}{\varphi_L} - \frac{1}{\varphi_*}\right)\left(\frac{\varphi_*^3}{3(1-\varphi_*)^3} - \frac{\varphi_L^3}{3(1-\varphi_L)^3}\right)}, \quad \varphi_L < \varphi_*, \\ u_* - u_R &= \sqrt{\left(\frac{1}{\varphi_*} - \frac{1}{\varphi_R}\right)\left(\frac{\varphi_R^3}{3(1-\varphi_R)^3} - \frac{\varphi_*^3}{3(1-\varphi_*)^3}\right)}, \quad \varphi_R < \varphi_*. \end{aligned} \tag{A.19}$$

The shock speeds are given by

$$s_1 = \frac{\varphi_* u_* - \varphi_L u_L}{\varphi_* - \varphi_L}, \quad s_2 = u_*, \quad \text{and} \quad s_3 = \frac{\varphi_R u_R - \varphi_* u_*}{\varphi_R - \varphi_*}. \tag{A.20}$$

These speeds must satisfy the Rankine-Hugoniot jump conditions, given by

$$\frac{[\varphi u]}{[\varphi]} = \frac{[\varphi u^2 + p]}{[\varphi u]} = \frac{[\omega_i u]}{[\omega_i]} = s. \tag{A.21}$$

When the following relation is verified:

$$-\sqrt{\left(\frac{1}{\varphi_R} - \frac{1}{\varphi_L}\right)\left(\frac{\varphi_L^3}{3(1-\varphi_L)^3} - \frac{\varphi_R^3}{3(1-\varphi_R)^3}\right)} < u_R - u_L < \left|\frac{1}{(1-\varphi_R)^2} - \frac{1}{(1-\varphi_L)^2}\right|, \quad \varphi_L > \varphi_R, \tag{A.22}$$

then the solution is 1-rarefaction/2-contact shock/3-shock, given by

$$\varphi = \begin{cases} \varphi_L, & -\infty < \eta \le \lambda_{1L}, \\ 1 - \left\{(1-\varphi_L)^{-2} + \lambda_{1L} - \eta\right\}^{-1/2}, & \lambda_{1L} < \eta < \lambda_{1*}, \\ \varphi_*, & \lambda_{1*} \le \eta < s_3, \\ \varphi_R, & s_3 < \eta < \infty, \end{cases} \tag{A.23}$$

$$u = \begin{cases} u_L, & -\infty < \eta \le \lambda_{1L}, \\ (1-\varphi_L)^{-1} + u_L - \left\{(1-\varphi_L)^{-2} + \lambda_{1L} - \eta\right\}^{1/2}, & \lambda_{1L} < \eta < \lambda_{1*}, \\ u_*, & \lambda_{1*} \le \eta < s_3, \\ u_R, & s_3 < \eta < \infty, \end{cases} \tag{A.24}$$

$$\omega_i = \begin{cases} \omega_{iL}, & -\infty < \eta \le \lambda_{1L}, \\ \dfrac{\omega_{iL}}{\varphi_L}\left\{1-\left\{\left(1-\varphi_L\right)^{-2}+\lambda_{1L}-\eta\right\}^{-1/2}\right\}, & \lambda_{1L} < \eta < \lambda_{1*}, \\ \omega_{i*} = \dfrac{\omega_{iL}\varphi_*}{\varphi_L}, & \lambda_{1*} \le \eta < u_*, \\ \omega_{i**} = \omega_{iR}\dfrac{\left(u_R - s_3\right)}{\left(u_* - s_3\right)}, & u_* < \eta < s_3, \\ \omega_{iR}, & s_3 < \eta < \infty, \end{cases} \tag{A.25}$$

with φ_* and u_* obtained from the following system:

$$\begin{aligned} u_* - u_L &= \frac{1}{1-\varphi_L} - \frac{1}{1-\varphi_*}, \quad \varphi_L > \varphi_*, \\ u_* - u_R &= \sqrt{\left(\frac{1}{\varphi_*}-\frac{1}{\varphi_R}\right)\left(\frac{\varphi_R^3}{3\left(1-\varphi_R\right)^3}-\frac{\varphi_*^3}{3\left(1-\varphi_*\right)^3}\right)}, \quad \varphi_R < \varphi_*. \end{aligned} \tag{A.26}$$

Finally, if the relation below is verified:

$$-\sqrt{\left(\frac{1}{\varphi_R}-\frac{1}{\varphi_L}\right)\left(\frac{\varphi_L^3}{3\left(1-\varphi_L\right)^3}-\frac{\varphi_R^3}{3\left(1-\varphi_R\right)^3}\right)} < u_R - u_L < \left|\frac{1}{\left(1-\varphi_R\right)^2}-\frac{1}{\left(1-\varphi_L\right)^2}\right|, \quad \varphi_L < \varphi_R, \tag{A.27}$$

then the solution is 1-shock/2-contact shock/3-rarefaction, given by

$$\varphi = \begin{cases} \varphi_L, & -\infty < \eta < s_1, \\ \varphi_*, & s_1 < \eta \le \lambda_{2*}, \\ 1-\left\{\left(1-\varphi_R\right)^{-2}-\lambda_{3R}+\eta\right\}^{-1/2}, & \lambda_{3*} < \eta < \lambda_{3R}, \\ \varphi_R, & \lambda_{3R} \le \eta < \infty, \end{cases} \tag{A.28}$$

$$u = \begin{cases} u_L, & -\infty < \eta < s_1, \\ u_*, & s_1 < \eta \le \lambda_{3*}, \\ -\left(1-\varphi_R\right)^{-1}+u_R+\left\{\left(1-\varphi_R\right)^{-2}-\lambda_{3R}+\eta\right\}^{1/2}, & \lambda_{3*} < \eta < \lambda_{3R}, \\ u_R, & \lambda_{3R} \le \eta < \infty, \end{cases} \tag{A.29}$$

$$\omega_i = \begin{cases} \omega_{iL}, & -\infty < \eta < s_1, \\ \omega_{i*} = \omega_{iL}\dfrac{\left(u_L - s_1\right)}{\left(u_* - s_1\right)}, & s_1 < \eta < u_*, \\ \omega_{i**} = \omega_{iR}\dfrac{\left(u_R - s_3\right)}{\left(u_* - s_3\right)}, & u_* < \eta < s_3, \\ \omega_{iR}, & s_3 < \eta < \infty, \end{cases} \tag{A.30}$$

with φ_* and u_* obtained from

$$\begin{aligned} u_* - u_L &= -\sqrt{\left(\frac{1}{\varphi_L} - \frac{1}{\varphi_*}\right)\left(\frac{\varphi_*^3}{3\left(1-\varphi_*\right)^3} - \frac{\varphi_L^3}{3\left(1-\varphi_L\right)^3}\right)}, \quad \varphi_L < \varphi_*, \\ u_* - u_R &= -\frac{1}{1-\varphi_R} + \frac{1}{1-\varphi_*}, \quad \varphi_R > \varphi_*. \end{aligned} \tag{A.31}$$